



Raman spectroscopy in graphene

L.M. Malard^a, M.A. Pimenta^a, G. Dresselhaus^b, M.S. Dresselhaus^{c,d,*}

^a Departamento de Física, Universidade Federal de Minas Gerais, Belo Horizonte-MG 30123-970, Brazil

^b Francis Bitter Magnet Laboratory, Massachusetts Institute of Technology, Cambridge, MA 02139-4307, USA

^c Department of Electrical Engineering and Computer Science, Massachusetts Institute of Technology, Cambridge, MA 02139-4307, USA

^d Department of Physics, Massachusetts Institute of Technology, Cambridge, MA 02139-4307, USA

ARTICLE INFO

Article history:

Accepted 13 February 2009

Available online 9 March 2009

editor: D.L. Mills

PACS:

78.30-j

61.48.De

73.20-k

71.38-k

ABSTRACT

Recent Raman scattering studies in different types of graphene samples are reviewed here. We first discuss the first-order and the double resonance Raman scattering mechanisms in graphene, which give rise to the most prominent Raman features. The determination of the number of layers in few-layer graphene is discussed, giving special emphasis to the possibility of using Raman spectroscopy to distinguish a monolayer from few-layer graphene stacked in the Bernal (AB) configuration. Different types of graphene samples produced both by exfoliation and using epitaxial methods are described and their Raman spectra are compared with those of 3D crystalline graphite and turbostratic graphite, in which the layers are stacked with rotational disorder. We show that Resonance Raman studies, where the energy of the excitation laser line can be tuned continuously, can be used to probe electrons and phonons near the Dirac point of graphene and, in particular allowing a determination to be made of the tight-binding parameters for bilayer graphene. The special process of electron–phonon interaction that renormalizes the phonon energy giving rise to the Kohn anomaly is discussed, and is illustrated by gated experiments where the position of the Fermi level can be changed experimentally. Finally, we discuss the ability of distinguishing armchair and zig-zag edges by Raman spectroscopy and studies in graphene nanoribbons in which the Raman signal is enhanced due to resonance with singularities in the density of electronic states.

© 2009 Elsevier B.V. All rights reserved.

Contents

1. Introduction.....	52
1.1. Types of graphene samples	52
1.2. Phonon dispersion of graphene	53
1.3. First-order Raman and double resonance Raman scattering in graphene.....	54
1.4. Group theory background	55
2. Raman spectroscopy experiments to learn about the number of layers and the stacking order in graphene systems.....	57
2.1. Raman spectra for monolayer graphene	57
2.2. Raman spectra for bilayer graphene.....	58
2.3. Raman spectra for trilayer graphene	59
2.4. Raman spectra for graphite	59
2.5. Raman spectra for turbostratic graphite	59
2.6. Stacking order	60

* Corresponding author at: Department of Physics, Massachusetts Institute of Technology, Cambridge, MA 02139-4307, USA.

E-mail address: millie@mgm.mit.edu (M.S. Dresselhaus).

3.	Resonance Raman studies: Probing electrons and phonons	62
3.1.	Monolayer graphene phonon dispersion	63
3.2.	Bilayer graphene phonon and electronic structure	64
4.	Raman studies on gated graphenes: Electron–phonon interaction.....	68
4.1.	Interaction of phonons with electron–hole pairs: Theoretical background	68
4.1.1.	Monolayer graphene	68
4.1.2.	Bilayer graphene	69
4.2.	Experimental results.....	70
4.2.1.	Monolayer graphene	70
4.2.2.	Bilayer graphene	70
5.	Raman studies of epitaxial graphene.....	73
5.1.	Raman characterization of SiC-derived graphene	73
5.2.	Raman characterization of CVD grown graphene	76
6.	Raman studies of graphene and graphite edges	78
7.	Raman studies of graphene nanoribbons	79
8.	Summary and conclusions.....	83
	Acknowledgments	84
	References.....	85

1. Introduction

Interest in studying the fundamental properties of graphene has grown in recent years since the discovery of an easy method to fabricate and identify these structures [1,2] and especially after the reports of the unusual quantum Hall effect in these systems [3,4]. Raman spectroscopy has historically played an important role in the structural characterization of graphitic materials [5–19], and has also become a powerful tool for understanding the behavior of electrons and phonons in graphene [20–25], aimed at gaining a better understanding of the information on graphene that we can get from Raman spectroscopy studies.

1.1. Types of graphene samples

Graphene consists of sp^2 carbon hexagonal networks, in which strong covalent bonds are formed between two adjacent carbon atoms. The unit cell for monolayer graphene (1-LG) contains two carbon atoms, A and B, each forming a triangular 2D network, but displaced from each other by the carbon–carbon distance $a_{C-C} = 0.142$ nm, as shown in Fig. 1(a).

The 3D graphite structure corresponds to a stacking of the hexagonal networks of individual graphene layers in the direction perpendicular to the layer plane (c -axis) in an AB (or Bernal) stacking arrangement, in which the vacant centers of the hexagons on one layer have carbon atoms on hexagonal corner sites on the two adjacent graphene layers, as shown in Fig. 1(b). In graphite with AB stacking, the unit cell consists of four carbon atoms A_1 , A_2 , B_1 , and B_2 on the two layer planes shown in Fig. 1(b). The in-plane and c -axis lattice constants for graphite are $a = 0.246$ nm and $c = 0.670$ nm, respectively. Normally, the bilayer graphene samples obtained from the mechanical exfoliation of graphite exhibit an AB stacking arrangement, and therefore the number of atoms in the unit cell of bilayer graphene (2-LG) is the same as that for graphite, with four atoms per unit cell, as shown in Fig. 1(b) and (c). Trilayer graphene (3-LG) in turn contains three layers, two of which are like bilayer graphene and the third layer has atom A_3 over A_1 and atom B_3 over B_1 as shown in Fig. 1(d). Four layer graphene (4-LG) consists of the stacking of two unit cells of the type shown in Fig. 1(c), one stacked on top of the other.

In reciprocal space, the unit cell is as shown in Fig. 1(e) for monolayer and bilayer (1-LG and 2-LG), and is planar, though atomic motion in the z direction normal to the plane would require a third direction. Fig. 1(e) also shows some high symmetry points within the first Brillouin zone of monolayer graphene: The Γ point at the zone center, the M points in the middle of the hexagonal sides and the K and K' points at the corners of the hexagons. Notice that K and K' are inequivalent since they are not connected by the unit vectors of the reciprocal lattice. In contrast, 3-LG and 4-LG reciprocal space requires a plane for $k_z = 0$ and $k_z = \pi/c$ forming the lower and upper planes of the Brillouin zone (BZ) for 3D graphite, as shown in Fig. 1(f).

In turbostratic graphite, denoted by 2D graphite, there is no stacking order between adjacent graphene layers and the interlayer spacing (>0.342 nm) is larger than that for crystalline graphite ($c/2 = 0.335$ nm). The absence of stacking order between the graphene planes results in 2D graphite having modified physical properties relative to 3D crystalline graphite. Crystalline 3D graphite is found in nature as a natural mineral, or is prepared from precipitants coming from steel-making, and these flakes are called “kish” graphite. Another common form of crystalline graphite is highly oriented pyrolytic graphite (HOPG), which is a synthetic AB stacked graphite obtained from carbon-based precursors, and heat treated at various high temperatures (over 3200 °C under pressure) [26].

Graphene samples in the early days of their study were mainly prepared by the mechanical exfoliation of HOPG graphite [1,2,27], although earlier preparation had occurred based on a nano-diamond precursor material [28]. Both of these graphene forms lead to multilayer graphene samples with AB Bernal stacking. An alternate route for the preparation of graphene

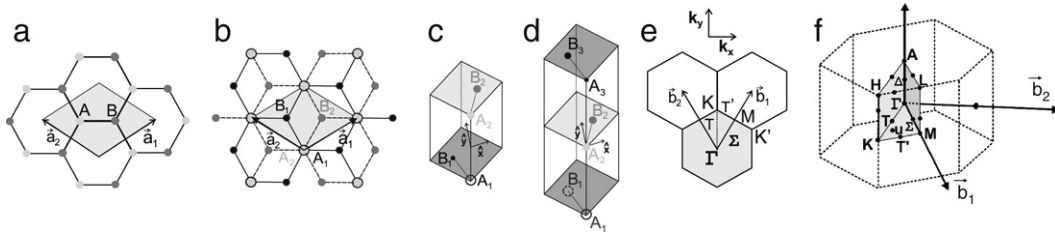


Fig. 1. (a) A top view of the real space unit cell of monolayer graphene showing the inequivalent atoms A and B and unit vectors \mathbf{a}_1 and \mathbf{a}_2 . (b) A top view of the real space of bilayer graphene. The light/dark gray dots and the black circles/black dots represent the carbon atoms in the upper and lower layers, respectively, of bilayer graphene (2-LG). (c) The unit cell and the \hat{x} and \hat{y} unit vectors of bilayer graphene and (d) the same as (c) but for trilayer graphene. (e) The reciprocal space unit cell showing the 1st Brillouin zone with its high symmetry points and lines, such as T connecting Γ to K ; Σ connecting Γ to M ; T' connecting K to M . The two primitive vectors \vec{b}_1 and \vec{b}_2 are shown and the two vectors on the top of the three hexagons show the reciprocal space coordinate axes. (f) The Brillouin zone for 3D graphite, showing the high symmetry points and axes. Here Δ is a high symmetry point along the axis connecting points A and Γ , and u is a point in the $KM\Gamma$ plane.

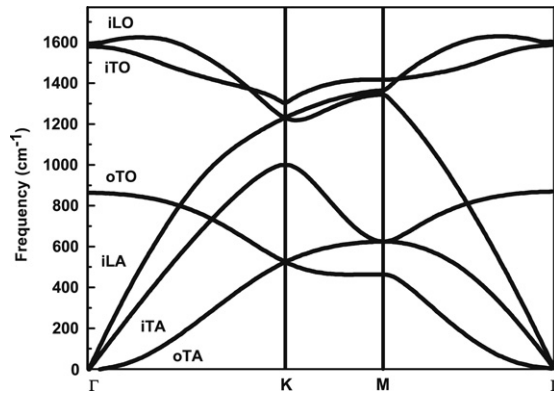


Fig. 2. (a) Calculated phonon dispersion relation of graphene showing the iLO, iT0, oTO, iLA, iTA and oTA phonon branches. (Adapted from Ref. [33]).

samples is from a SiC-based precursor method [29,30], leading to a graphene family of materials with significant interaction with the SiC substrate, thereby having somewhat different properties, including only partial stacking order. Epitaxial chemical vapor deposition (CVD) growth of graphene using various transition metal catalysts, such as Ni, has also been demonstrated [31], and this class of materials is still under active development. Experiments described in this review are carried out on graphene samples sitting on various substrates (like Si/SiO₂), freely suspended, chemically doped or gated to control the Fermi level. Freely suspended graphene tends to have higher mobility than its graphene counterparts on substrates [32].

1.2. Phonon dispersion of graphene

An understanding of the phonon dispersion of graphene is essential to interpret the Raman spectra of graphene. Since the unit cell of monolayer graphene contains two carbon atoms, A and B, there are six phonon dispersion bands (see Fig. 2), in which three are acoustic branches (A) and the other three are optic (O) phonon branches. For one acoustic branch (A) and one optic (O) phonon branch, the atomic vibrations are perpendicular to the graphene plane, and they correspond to the out-of-plane (o) phonon modes. For two acoustic and two optic phonon branches, the vibrations are in-plane (i). Traditionally, the directions of the vibrations are considered with respect to the direction of the nearest carbon–carbon atoms and, therefore, the phonon modes are classified as longitudinal (L) or transverse (T) according to vibrations parallel with or perpendicular to, respectively, the A–B carbon–carbon directions. Therefore, along the high symmetry ΓM and ΓK directions, the six phonon dispersion curves are assigned to LO, iT0, oTO, LA, iTA, and oTA phonon modes. (see Fig. 2)

Near the zone center (Γ point), the in-plane iT0 and LO optic modes correspond to the vibrations of the sublattice A against the sublattice B, and these modes are degenerate at the Γ point. According to Group Theory (see Section 1.4), the degenerate zone-center LO and iT0 phonon modes belong to the two-dimensional E_{2g} representation and, therefore, they are Raman active modes [8,34]. The degeneracy of the LO and iT0 phonons disappears for points inside the first Brillouin zone (BZ) of graphene. Along the Γ – K line, the LO and iT0 branches will have T_3 and T_1 symmetries, respectively, whereas the symmetries of these branches along the Γ – M line are Σ_3 and Σ_1 , respectively [35,36].

The phonon modes around the K point are especially important, since the D -band and G' -band are related to phonon modes in the vicinity of the K point. Exactly at the K -point, the phonon which comes from the iT0 branch is non-degenerate

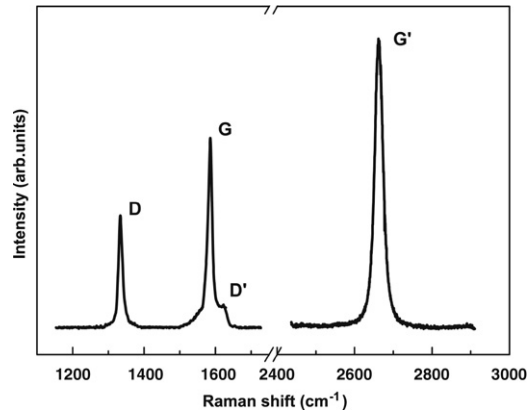


Fig. 3. Raman spectrum of a graphene edge, showing the main Raman features, the D , G and G' bands taken with a laser excitation energy of 2.41 eV.

and belongs to the A'_1 irreducible representation of the point group D_{3h} . The LO and LA phonon branches meet each other at the K point giving rise to a doubly degenerate phonon, with E' symmetry [37,38].

Finally, to correctly describe the dispersion of the LO and iTO phonon branches near the Γ and K points, it is important to consider the renormalization of the phonon energies, associated with a process in which a phonon can create an electron–hole pair (similarly to the creation of an electron–positron pair by a photon in quantum electrodynamics) [39]. This important electron–phonon coupling cannot be understood within the framework of the Born–Oppenheimer approximations, and gives rise to an interesting effect known as the Kohn anomaly [40]. The Kohn anomaly is responsible for a softening of certain Γ and K point phonons [41].

In 3D graphite, there is a phonon dispersion along the c direction perpendicular to the plane. For few layer graphene (F-LG), we have a finite number of graphene planes, and several of the in-plane phonon branches are now split by discrete wave vectors in the c direction. In the case of bilayer graphene, the phonon branches of monolayer graphene split into two branches, which correspond to the in-phase (symmetric) or out-of-phase (anti-symmetric) vibrations of the atoms in the two different layers.

1.3. First-order Raman and double resonance Raman scattering in graphene

The most prominent features in the Raman spectra of monolayer graphene are the so-called G band appearing at 1582 cm^{-1} (graphite) and the G' band at about 2700 cm^{-1} using laser excitation at 2.41 eV (see for example, Fig. 3). In the case of a disordered sample or at the edge of a graphene sample, we can also see the so-called disorder-induced D -band, at about half of the frequency of the G' band (around 1350 cm^{-1} using laser excitation at 2.41 eV).

The G band is associated with the doubly degenerate (iTO and LO) phonon mode (E_{2g} symmetry) at the Brillouin zone center. In fact, the G -band is the only band coming from a normal first order Raman scattering process in graphene. On the other hand, the G' and D -bands originate from a second-order process, involving two iTO phonons near the K point for the G' band or one iTO phonon and one defect in the case of the D -band. Since the G' band is approximately twice the D band frequency ($\omega_{G'} \sim 2\omega_D$), some authors prefer to call it the 2D band. However, this two-phonon band is allowed in the second-order Raman spectra of graphenes without any kind of disorder or defects. In order to prevent any misleading connection of this feature with disorder or defects, and to avoid confusion between the designation of “2D” to denote two dimensionality, we will use here the conventional notation “ G' -band” as is used in the graphite and nanotube literature. We use the notation D' -band to denote another weak disorder-induced feature which appears at $\sim 1620\text{ cm}^{-1}$, as is discussed further below.

Both the D and G' bands exhibit a dispersive behavior since their frequencies in the Raman spectra change as a function of the energy of the incident laser, E_{laser} . The D -band frequency ω_D upshifts linearly with increasing E_{laser} over a wide laser energy range, the slope of $(\partial\omega_D/\partial E_{\text{laser}})$ being about $50\text{ cm}^{-1}/\text{eV}$. The slope of $(\partial\omega_{G'}/\partial E_{\text{laser}})$ is about twice that of the D -band, i.e., around $100\text{ cm}^{-1}/\text{eV}$ [42–44].

The origin and the dispersive behavior in the frequency of the D and G' bands originate from a double resonance (DR) Raman process [45–47]. In this DR process, the wave-vectors q of the phonons associated with the D and G' bands (measured from the K point) would couple preferentially to the electronic states with wave-vectors k (measured from the K point), such that $q \simeq 2k$.

The double-resonance (DR) process shown in the center and right side of Fig. 4 begins with an electron of wave-vector \mathbf{k} around K absorbing a photon of energy E_{laser} . The electron is inelastically scattered by a phonon or a defect of wavevector \mathbf{q} and energy E_{phonon} to a point belonging to a circle around the K' point, with wavevector $\mathbf{k} + \mathbf{q}$, where the K' point is related to K by time reversal symmetry [36]. The electron is then scattered back to a \mathbf{k} state, and emits a photon by recombining with a hole at a \mathbf{k} state. In the case of the D band, the two scattering processes consist of one *elastic* scattering event by defects of the crystal and one *inelastic* scattering event by emitting or absorbing a phonon, as shown in Fig. 4. In the case

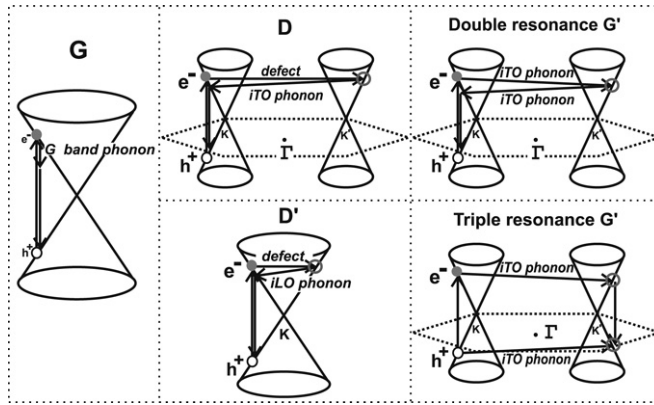


Fig. 4. (Left) First-order G -band process and (Center) one-phonon second-order DR process for the D -band (intervalley process) (top) and for the D' -band (intravalley process) (bottom) and (Right) two-phonon second-order resonance Raman spectral processes (top) for the double resonance G' process, and (bottom) for the triple resonance G' band process (TR) for monolayer graphene [6]. For one-phonon, second-order transitions, one of the two scattering events is an elastic scattering event. Resonance points are shown as open circles near the K point (left) and the K' point (right).

of the G' -band, both processes are *inelastic* scattering events and two phonons are involved. This double resonance mechanism is called an *intervalley* process because it connects points in circles around inequivalent K and K' points in the first Brillouin zone of graphene. On the other hand, the double resonance process responsible for the D' band ($\sim 1620 \text{ cm}^{-1}$) is an *intra-valley* process, since it connects two points belonging to the same circle around the K point (or the K' point) [47,48].

In principle, many different initial electronic states around the K point (or Dirac point) and phonons with different symmetries and wavevectors can satisfy the DR condition. However, due to: (1) the existence of singularities in the density of phonon states which satisfy the DR condition, (2) the angular dependence of the electron–phonon scattering matrix elements, and (3) the destructive interference effects when the Raman transition probability is calculated, only a few specific DR processes contribute strongly to the Raman G' and D bands [49]. For example, only *iTO* and *iLO* branches are observed in the intervalley and intravalley DR processes, respectively, because the corresponding phonons are strongly coupled to electrons along the high-symmetry directions associated with the singularities in the DR phonon density of states [37,47, 48,50–52].

When E_{laser} is increased relative to the Dirac point, the resonance k vector for the electron moves away from the K point. In the DR process, the corresponding q vector for the phonon increases with increasing k , as measured from the K point. Thus by changing the laser energy, we can observe the phonon energy $\hbar\omega(q)$ along the phonon dispersion relations (Fig. 2). This effect is observed experimentally as a dispersion of the phonon energy as a function of E_{laser} [48]. A tunable laser system can directly show this dispersive behavior for the D -band and G' -band in the Raman spectrum.

In a DR Raman process, two resonance conditions for three scattering events should be satisfied, in which the intermediate $\mathbf{k} + \mathbf{q}$ state is always a real electronic state and either the initial or the final \mathbf{k} state is a real electronic state [53]. However, the Raman process can also occur by scattering of holes. In the special case of graphene, where the valence and conduction bands are almost mirror bands of one another relative to the Fermi energy, this can lead to an important effect, that is the triple resonance (TR) Raman process [54]. For example, the TR process in Fig. 4, shows that we can consider, instead of the electron being scattered back by a phonon with wavevector $-\mathbf{q}$, that the hole will be scattered by a wavevector $+\mathbf{q}$. In this case, the electron–hole generation is a resonant process, in which both the electron and hole scattering processes will be resonant, and finally the electron–hole recombination at the opposite side with respect to the K point will also occur near the K' point between an electron and a hole in resonance states. Therefore, for the triple resonance process all steps in the usual double resonance process now become resonant. This triple-resonance condition might explain why the G' -band is more intense than the G -band in monolayer graphene. Park et al. [55] have shown that the large intensity of the G' -band for monolayer graphene can also be explained within the context of the DR formalism.

1.4. Group theory background

In this section we review the symmetry properties for monolayer (1-LG), bilayer (2-LG) and trilayer (3-LG) graphene giving emphasis to high symmetry lines which are important to address the DR phenomena (see Section 1.3). These symmetry considerations support the experimental observations of the G' band lineshape which sensitively depends on the number of graphene layers, as given in Section 2.

Monolayer graphene (Fig. 1(a)) is described by the space group $P6/mmm (D_{6h}^1)$ in the Hermann–Mauguin (Schoenflies) notation. At the Γ point, the group of the wavevector (GWV) is isomorphic to the point group D_{6h} (the Schoenflies character tables for the point groups can be found in Ref. [36]).

The real space structures for bilayer and trilayer graphene with AB Bernal stacking are shown in Fig. 1(b, c) and (d), respectively. The symmetries for N -layer graphene, with N even or odd ($N \neq 1$), are the same as for bilayer and trilayer

Table 1

The space groups and wavevector point groups for monolayer, N -layer graphene and graphite at all points in the Brillouin zone.

	Space group	Γ	K (K')	M	T (T')	Σ	U
Monolayer	$P6/mmm$	D_{6h}	D_{3h}	D_{2h}	C_{2v}	C_{2v}	C_{1h}
N even	$P\bar{3}m1$	D_{3d}	D_3	C_{2h}	C_2	C_{1v}	C_1
N odd	$P\bar{6}m2$	D_{3h}	C_{3h}	C_{2v}	C_{1h}	C_{2v}	C_{1h}
N infinite	$P6_3/mmc$	D_{6h}	D_{3h}	D_{2h}	C_{2v}	C_{2v}	C_{1h}

Table 2

The irreducible representations for the lattice vibrations $\Gamma_{\text{lat.vib.}}$ for monolayer, bilayer and trilayer graphene at the Γ point and along the T (T') lines.

	Monolayer	Bilayer	Trilayer
Γ	$\Gamma_2^- + \Gamma_5^- + \Gamma_4^+ + \Gamma_6^+$	$2(\Gamma_1^+ + \Gamma_3^+ + \Gamma_2^- + \Gamma_3^-)$	$2\Gamma_1^+ + 4\Gamma_2^- + 4\Gamma_3^+ + 2\Gamma_3^-$
T (T')	$2T_1 + T_2 + 2T_3 + T_4$	$6(T_1 + T_2)$	$10T^+ + 8T^-$

Table 3

The irreducible representations for the group of the wavevector Γ_π for monolayer, bilayer and trilayer graphene along the T (T') line.

	Monolayer	Bilayer	Trilayer
T (T')	$T_2 + T_4$	$2(T_1 + T_2)$	$2T^+ + 4T^-$

graphene, respectively. The symmetry operations that distinguish the point groups between even and odd layers are the horizontal mirror planes, which are absent for N even, and the inversion operation, which is absent for N odd [56]. The point groups isomorphic to the GWV for monolayer graphene, N -layer graphene (N even and odd), and for N infinite (graphite) are listed in Table 1 for all points and lines in the first Brillouin zone (BZ) as shown in Fig. 1(e). The irreducible representations for the lattice vibrations ($\Gamma_{\text{lat.vib.}}$) and for the π electrons (Γ_π) at the Γ point and along the T and T' lines ($K\Gamma$ and KM directions, respectively) in the first BZ for the $\Gamma_{\text{lat.vib.}}$ are found in Table 2 and for the Γ_π in Table 3. A more complete group theory analysis for every high symmetry point inside the first BZ and depending on layer number can be found in Ref. [56].

The first order Raman process occurs at the Γ point due to momentum conservation. Then the Raman-active modes can be found by looking at the quadratic form of the basis function corresponding to the $\Gamma_{\text{lat.vib}}$ representation. The Raman-active modes can then be summarized as follows for monolayer (1-LG), bilayer (2-LG) and trilayer (3-LG) graphene [56]:

$$\Gamma^{\text{Raman}} = \Gamma_6^+, \quad \text{for 1-LG} \quad (1)$$

$$\Gamma^{\text{Raman}} = 2\Gamma_3^+ + 2\Gamma_1^+, \quad \text{for 2-LG} \quad (2)$$

$$\Gamma^{\text{Raman}} = 3\Gamma_3^+ + 2(\Gamma_3^- + \Gamma_1^+), \quad \text{for 3-LG.} \quad (3)$$

In monolayer graphene 1-LG the Raman G band is ascribed to a doubly degenerate Γ_6^+ symmetry mode. In bilayer graphene the G band belongs to the Γ_3^+ irreducible representation, which is doubly degenerate and represents the atomic motion of nearest neighbor carbon atoms moving against each other within the plane and in phase between the two layers; we call this mode the symmetric (S) G mode. The Γ_3^- representation, which is not Raman active in bilayer graphene, due to the center of inversion symmetry in the D_{3h} point group, can become active if this inversion symmetry operation is broken. The Γ_3^- mode is also represented by the atomic motion of the nearest neighbor carbon atoms moving against each other within the plane, but out-of-phase between the two layers, and we call this the antisymmetric (AS) G band. In Section 4 we show that this AS Raman mode can be activated in bilayer graphene by lowering its symmetry. There is also a low frequency Γ_3^+ mode (35 – 53 cm^{-1}) with a frequency depending on the number of layers [57]. The other two Γ_1^+ irreducible representations give rise to Raman modes near ~ 80 cm^{-1} and ~ 900 cm^{-1} [57,58]. For trilayer graphene, the G band is assigned to a combination of Γ_3^+ and Γ_3^- representations, and also the Γ_1^+ representation is Raman active with a lower frequency component, as in bilayer graphene.

To address the double resonance process, first we find the allowed absorption transitions ($W(\mathbf{k})$) between the valence ($\psi^v(\mathbf{k})$) and conduction ($\psi^c(\mathbf{k})$) bands in the electric-dipole approximation. For each of the Γ_π representations found in Table 3, we calculate the electron–radiation interaction by noting that $W(\mathbf{k}) \propto |\mathbf{P} \cdot \langle \psi^c(\mathbf{k}) | \nabla | \psi^v(\mathbf{k}) \rangle|^2$, where \mathbf{P} is the polarization vector of light which is described by an irreducible representation which contains the (x , y or z) basis function. Along the T line where the absorption of light occurs in the Raman process, we list in Table 4 the symmetry-allowed electron–radiation interactions for monolayer, bilayer and trilayer graphene [56].

From the possible electron–hole creation pairs that obey the symmetry requirements as given above, the symmetry of the DR processes can be evaluated as being a scattering process which is mainly associated with the electronic T lines near the K and K' points and the phonons along the T' line [52]. The symmetry of the electron–phonon (el–ph) scattering process is calculated from the initial and final electron wave functions coupled by the phonon eigenvector [59,60]. Therefore, the selection rules for the DR processes are obtained by the direct product of the symmetries of the initial and final electronic

Table 4

Selection rules for the electron–radiation interaction in optical absorption along the T line with x and y polarized light in monolayer, bilayer and trilayer graphene (x and y polarized light are in the same direction as the definition of k_x and k_y in Fig. 1(e)).

	Polarization	$W(k)$
Monolayer	$x \in T_3$	$T_2 \otimes T_3 \otimes T_4$
Bilayer	$x \in T_2$	$T_1 \otimes T_2 \otimes T_2$
		$T_2 \otimes T_2 \otimes T_1$
	$y \in T_1$	$T_1 \otimes T_1 \otimes T_1$
		$T_2 \otimes T_1 \otimes T_2$
Trilayer	$x, y \in T^+$	$T^+ \otimes T^+ \otimes T^+$
		$4 \times (T^- \otimes T^+ \otimes T^-)$

Table 5

Allowed DR processes for monolayer, bilayer and trilayer graphene along the T line for each phonon symmetry along the T' line.

	Phonon	Allowed scattering
Monolayer	T_1	$T_4 \rightarrow T_4$
Bilayer	T_1	$T_1 \rightarrow T_1, T_2 \rightarrow T_2$
	T_2	$T_1 \rightarrow T_2, T_2 \rightarrow T_1$
Trilayer	T^+	$T^+ \rightarrow T^+, T^- \rightarrow T^-$
	T^-	$T^+ \rightarrow T^-$

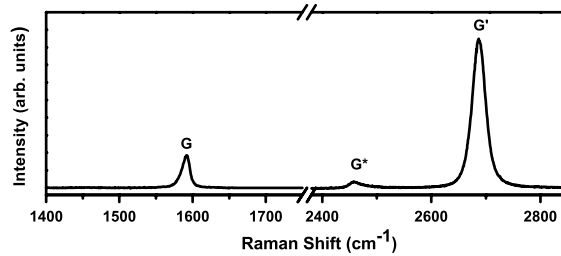


Fig. 5. Measured Raman spectrum with 2.41 eV laser excitation energy, showing the first-order Raman allowed G band and the very strong G' band of monolayer graphene which is described by one Lorentzian and a peak frequency of 2687 cm^{-1} [63], the G^* Raman band is also shown near $\sim 2450 \text{ cm}^{-1}$.

states and the symmetry of the phonon involved in the process. The symmetry-allowed DR processes for monolayer, bilayer and trilayer graphene along the high symmetry line ΓK with phonons along the KM direction are found in Table 5 [56].

The selection rules for the DR phenomena found in Table 5, will be used in Section 2 for understanding the evolution of the number of peaks in the G' band as a function of the number of layers in AB stacked graphene.

2. Raman spectroscopy experiments to learn about the number of layers and the stacking order in graphene systems

In the case of Bernal AB stacking of graphene (see Section 1.1), Ferrari et al. [20] showed that is possible to use the second order G' feature in the Raman spectra of graphene to learn about the number of layers in a graphene sample. As in other sp^2 carbons, the G' feature in the Raman spectrum originates from the double resonance (DR) Raman process [61,62], and links electrons and phonons in the graphene dispersion relations [20,24,25,52,63].

2.1. Raman spectra for monolayer graphene

Starting from monolayer graphene (1-LG), we first consider the DR process which is depicted in Fig. 4 (see Section 1.3). Here we see that the selection rules discussed in Section 1.3 for electron–phonon scattering occurring along the $K\Gamma K'$ direction have to satisfy the scattering process shown in Fig. 4, as further discussed below [52,61,64]. But first we show in Fig. 5 a Raman spectrum measured with a laser energy of 2.41 eV for a monolayer graphene sample, showing the G and G' bands. The G' band for 1-LG at room temperature exhibits a single Lorentzian feature with a full width at half maximum (FWHM) of $\sim 24 \text{ cm}^{-1}$. What is remarkable about this spectrum is the large intensity of the G' band relative to the G -band, and this large relative intensity of the G' band can be understood in terms of a triple resonance process shown in Fig. 4. This is a unique spectrum for all sp^2 carbons where all steps in the process (see Fig. 4) are resonant because of the linear $E(k)$ dispersion.

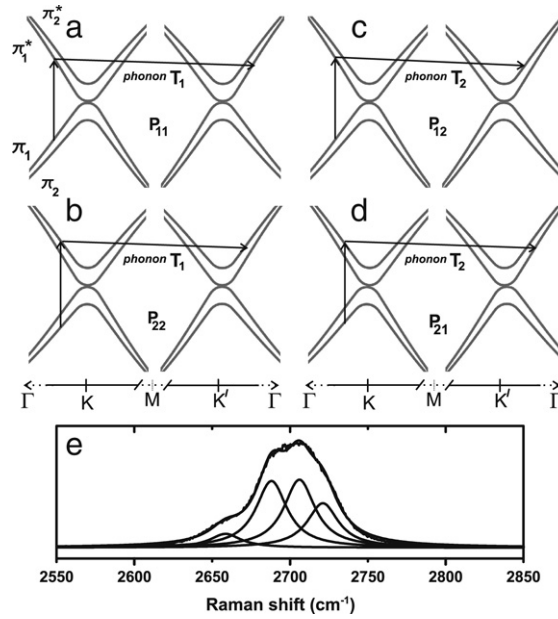


Fig. 6. Schematic view of the electron dispersion of bilayer (2-LG) graphene near the K and K' points showing both π_1 and π_2 bands. The four DR processes are indicated: (a) process P_{11} , (b) process P_{22} , (c) process P_{12} , and (d) process P_{21} . The phonon symmetries are also indicated for each process. (e) The measured G' Raman band of bilayer graphene for 2.41 eV laser energy. The four fitted Lorentzians are also shown with peak frequencies at 2658, 2688, 2706, and 2721 cm^{-1} , respectively [63].

2.2. Raman spectra for bilayer graphene

In the case of bilayer graphene (2-LG) with Bernal AB layer stacking, both the electronic and phonon bands split into two components with special symmetries. For these two phonon components, the motion of the carbon atoms in the upper and lower layers correspond to different irreducible representations, such that the motion in the two layers are in phase with respect to each other for one component and out of phase for the other component. The electrons in 2-LG have a parabolic $E(k)$ dispersion relation showing a k^2 dependence near $k = 0$ and have two conduction and two valence bands [22,65–67] as shown in Fig. 6. The electrons are also affected by the interlayer interaction and they also split into symmetric and anti-symmetric symmetry components. For the case of 2-LG, the DR conditions are more complex than in the case of monolayer graphene (1-LG) where there is only one main DR process contributing to the G' band. From a group theory analysis [36, 56,68], bilayer graphene is isomorphic to the D_{3d} point group at the Γ point. Consequently, the appropriate group of the wave vector for the high symmetry ΓK axis (also called the T axis) is the C_2 point group following the notation used for the graphite space group #194 (see Section 1.4) [36,56,68].

Fig. 6(a) shows a schematic view of the bilayer graphene electronic structure where the upper (lower) and lower (upper) branches of the valence (conduction) band are labeled as π_1 (π_1^*) and π_2 (π_2^*), respectively [22]. The major steps of the DR process occur along the T line (ΓK) along which the π_2 and π_1^* bands belong to the T_1 totally symmetric irreducible representation, while the π_1 and π_2^* have odd T_2 symmetry [36]. The light absorption selection rules for both x and y light polarizations [36] result in electron–hole creation between $\pi_1 \rightleftharpoons \pi_1^*$ and $\pi_2 \rightleftharpoons \pi_2^*$ bands for x light polarization, and between $\pi_1 \rightleftharpoons \pi_2^*$ and $\pi_2 \rightleftharpoons \pi_1^*$ bands for y light polarization (see Section 1.4). Here k_x is along ΓM and k_y is along ΓK (see Fig. 1(e)). Because of the dependence of k on the polarization direction in graphene [69], the calculated contribution of the y light polarization for the electron–hole creation is expected to be weaker compared to that for the x polarization [68].

Now, for computing the number of resonant conditions involved in the DR process, we are left with electrons in only two excited electronic states with wave vectors near the K point, from which the electrons will then be scattered by a phonon to an electron state with a wave vector near the K' point. This electron–phonon scattering can now occur with two phonons with symmetries T_1 and T_2 . For the case of a T_1 phonon and the electron initial state in band π_1^* (T_2 symmetry) or π_2^* (T_1 symmetry), the scattering can occur between the $\pi_1^* \rightarrow \pi_1^*$ or $\pi_2^* \rightarrow \pi_2^*$ bands, respectively. The corresponding symmetry-allowed scattering process by a T_2 phonon will connect bands of different symmetries, i.e., $\pi_1^* \rightleftharpoons \pi_2^*$, where in all cases the matrix element is invariant for a symmetry-allowed process.

These four different P_{ij} processes are depicted in Fig. 6(a–d), where i (j) denotes an electron scattered from (to) each conduction band $\pi_{i(j)}^*$. The P_{11} and P_{22} processes come from an iTO phonon with S T_1 symmetry, while the P_{12} and P_{21} processes come from an iTO phonon with AS T_2 symmetry. These four different scattering processes give rise to four Raman peaks in the G' spectrum. Fig. 6(e) shows the Raman spectra of a bilayer graphene sample with AB stacking, where the spectra were fitted with four Lorentzians [63], each with a FWHM of $\sim 24 \text{ cm}^{-1}$. If the valence and conduction bands were

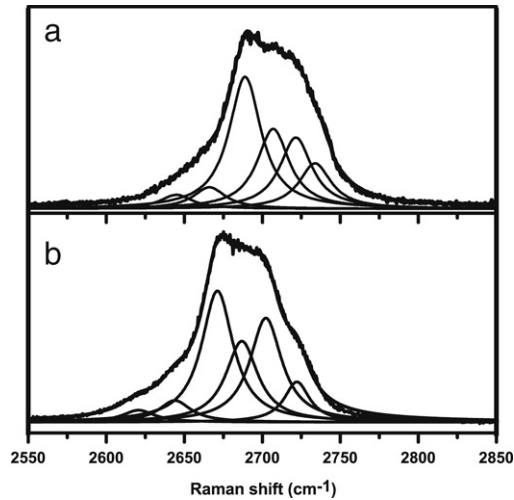


Fig. 7. (a) Measured trilayer (3-LG) graphene with 2.41 eV laser energy and fitted with 6 Lorentzians. (b) Measured trilayer graphene with 2.18 eV laser energy, showing that 6 Lorentzians are needed to fit the G' feature for 3-LG.

mirror images of one another, then processes P_{12} and P_{21} would be degenerate. Experimentally the fitting to four bands gives a better fit, suggesting that asymmetries between the valence and conduction band are present in 2-LG.

2.3. Raman spectra for trilayer graphene

Making the same group theory analysis for trilayer graphene, we can show that the number of allowed Raman peaks in the G' band is fifteen [56]. Trilayer graphene is isomorphic to the D_{3h} point group at the Γ point, and has six atoms in the unit cell. Then along the T axis connecting $\Gamma-K$, the electronic representation is given by $2T^+ + 4T^-$ in the C_{1h} point group which describes the group of the wave vector along $\Gamma-K$ for an odd number of graphene layers (see Table 3). Both the x and y components of the light polarization vector in this case are represented by a totally symmetric representation T^+ , so we are left with five possible electron-hole creation transitions connecting the valence and conduction bands with the same symmetry. The electron-phonon scattering from K to K' will occur by three different iTO phonon branches, one with T^+ and two of them with T^- symmetries. Each of the five possible excited electrons can be scattered by each of these phonons to three different conduction bands at the K' point, so that by summing all possibilities, we will have fifteen different processes.

To correctly identify the G' Raman band lineshape for trilayer graphene, one should model the DR Raman process, by considering 15 different transitions, but the energy separations of many of these fifteen different processes turn out to be very close to each other from an experimental standpoint. Experimentally it is found that the minimum number of peaks with a FWHM of $\sim 24 \text{ cm}^{-1}$ necessary to correctly fit the G' in this case is six as shown in Fig. 6(a) and (b) for $E_{\text{laser}} = 2.41$ and 2.18 eV, respectively. In fact one could use even fewer peaks to fit the G' feature of 3-LG [21] for $E_{\text{laser}} = 2.41$ eV. However, for lower laser energies, the splitting of the G' peak needs at least six peaks (see Fig. 7(b)). Another important point here is the fact that the same FWHM of $\sim 24 \text{ cm}^{-1}$ is always used for the G' band which comes from the monolayer graphene feature, thereby defining a characteristic lifetime for the DR Raman process.

2.4. Raman spectra for graphite

The G' band continues to evolve with the number of graphene layers until we reach the final material that we must consider which is bulk graphite. For highly oriented pyrolytic graphite (HOPG) (see Section 1.3) we can describe the G' band with two peaks (see Fig. 8(e)). Fig. 8 compares the Raman spectra in the G' band region for (a) monolayer, (b) bilayer, (c) trilayer, (d) four layer graphene and (e) HOPG, showing the evolution of the Raman spectra with the number of layers. Cançado et al. [68] attributed the G' band for HOPG to come from a convolution of peaks along the entire k_z axis ranging from $k_z = 0$ to $k_z = \pi/c$. The higher frequency and most intense peak comes mainly from the P_{11} DR Raman process [68]. The turning point of the Raman spectra, distinguishing the G' band for HOPG from that for few-layer graphene, starts to happen at 4-LG, where the experimental analysis is here given in terms of 3 peaks. From Fig. 8(d) it is possible to see that now the high frequency side of the G' band has a larger intensity than that for fewer graphene layers, indicating the passage to HOPG, which has its higher intensity peak at higher frequencies.

2.5. Raman spectra for turbostratic graphite

It is important to note that the identification of the number of layers by Raman spectroscopy is well established only for graphene samples that have AB Bernal stacking. Graphene samples made by the mechanical exfoliation of natural or HOPG

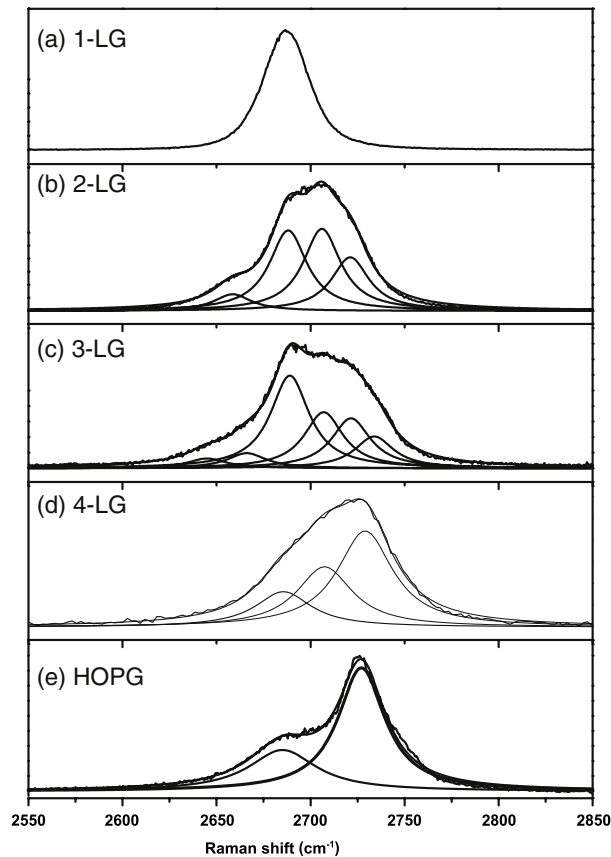


Fig. 8. The measured G' Raman band with 2.41 eV laser energy for (a) 1-LG, (b) 2-LG, (c) 3-LG, (d) 4-LG, (e) HOPG and (f) turbostratic graphite. The splitting of the G' Raman band opens up in going from mono- to three-layer graphene and then closes up in going from 4-LG to HOPG.

graphite lead to graphene flakes that have predominantly AB stacking, but this is not necessarily the case for graphene samples made by other growth methods (see Section 5).

For example, turbostratic graphite, in which the stacking of the graphene layers is rotationally random with respect to one another along the c axis (see Section 1.1), shows a Raman G' band that is a single Lorentzian (see Fig. 8(f)), just as in monolayer graphene (see Section 2.1) but with a larger linewidth. The absence of an interlayer interaction between the graphene planes makes the Raman spectra of turbostratic graphite look much like that for monolayer graphene, but now with a broadening of the G' feature due to the relaxation of the DR Raman selection rules associated with the random orientation of the graphene layers with respect to each other. This is reflected in the Raman spectra of the G' band as a single Lorentzian, just as in monolayer graphene, but now for turbostratic multilayer graphene with a FWHM of $\sim 45\text{--}60\text{ cm}^{-1}$ [70,71] instead of $\sim 24\text{ cm}^{-1}$, as is found for monolayer graphene. Also the relative intensity of the G' feature to that of the G -band $I_{G'}/I_G$ is much smaller for turbostratic graphite and the frequency is upshifted from that of 1-LG.

We have shown in this section how the G' -band lineshape can be used to determine the number of layers of a graphene sample with AB stacking. Raman spectroscopy thus provides a useful and fast method to quantify the number of graphene layers and also provides some information about the stacking order. Also we explained the origin of the number of peaks in the G' band that is associated with differences in the electronic and phonon dispersion relations, that depend on the number of layers in N -LG. Group theory analysis helps us to understand the relation between the number of layers and the number of peaks in the G' -band that can be expected. Layer stacking is shown to play a vital role in the group theory analysis of the G' band spectra [56].

2.6. Stacking order

Next, we give an overview of experiments to measure the stacking order using Raman spectroscopy in graphite, and then we move to graphene systems, where it is possible to clearly observe the changes in the lineshape of the G' Raman band associated with interplanar stacking order to study topics such as in-plane crystallite size [9,10,72] and out-of-plane stacking order [14,15,17,71]. In this section we will focus on what Raman spectra tell us about the out-of-plane stacking order of graphene layers. Such knowledge is important for understanding related defects and disorder in few-layer graphenes (F-LG).

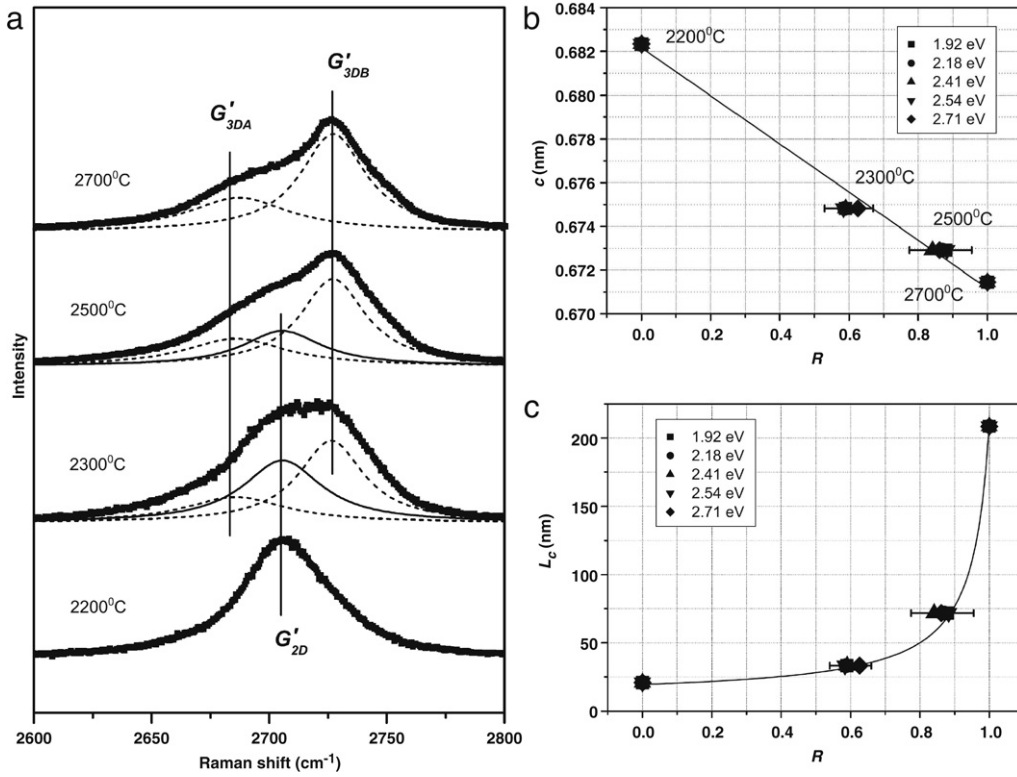


Fig. 9. (a) The G' Raman spectra of partially disordered graphite samples heat-treated at different temperatures. The spectra were taken with 2.41 eV laser energy. By heat treatment of the sample at high temperatures, the G' band goes from a one-peak (G'_{2D}) to a two peak (G'_{3DA} and G'_{3DB}) profile. (b) The average of the out-of-plane lattice parameter c for the different samples obtained from X-ray diffraction analysis vs. the ratio R in Eq. (4) for five different laser excitation energies. (c) The average of the out-of-plane crystallite thickness L_c of the different samples obtained from the X-ray diffraction analysis vs. the ratio R in Eq. (4) for different laser excitation energies. Figure adapted from Ref. [71].

Recent Raman experiments on disordered graphite films heat-treated at different temperatures, showed that the G' Raman band can be used to infer information about the out-of-plane lattice parameter (c) and the interplanar crystalline coherence length (L_c) [71]. Fig. 9(a) shows the Raman spectra in the G' spectral band region, for four different samples treated at different temperatures. The sample heat-treated at 2200 °C shows a typical spectrum of a turbostratic graphite, consisting of only one Lorentzian component (G'_{2D}). On the other hand, the spectrum for the sample heat treated at the higher temperature of 2700 °C shows a characteristic G' spectrum of graphite, with two Lorentzians (G'_{3DA} and G'_{3DB}). The two samples with intermediate heat treatment temperatures in Fig. 9(a) show spectra evolving from a G' Raman band characteristic of turbostratic graphite (2200 °C) to a G' band characteristic of HOPG, with the spectra in the intermediate temperature range show the coexistence of G'_{2D} , G'_{3DA} and G'_{3DB} Raman bands. Considering that a volume V is illuminated by the laser beam, we can write $V = V_{3D} + V_{2D}$, where V_{3D} (V_{2D}) is the 3D (2D) graphite part of the total volume V . The fractional 3D volume is given by the ratio $R = V_{3D}/V$ which can be obtained experimentally from the intensity (I) of the G' spectra as [71]:

$$R = \frac{I_{G'_{3DB}}}{I_{G'_{3DB}} + I_{G'_{2D}}} \quad (4)$$

and correspondingly the 2D volume ratio becomes $V_{2D}/V = 1 - R$. By comparing the experimental value of R for the various samples in Fig. 9(a) and the value of the c -axis lattice constant c obtained by X-ray diffraction analysis, Cañado et al. [71] derived an empirical formula from a linear fit of Fig. 9(b) for extracting an experimental value of c for samples with varying amounts of c -axis stacking faults by Raman spectroscopy [71]:

$$c(\text{nm}) = 0.682 - 0.11R. \quad (5)$$

Thus Eq. (5) allows a determination of the out-of-plane lattice parameter from Raman spectroscopy using laser excitation lines in the visible range. Moreover, the combination of X-ray diffraction analysis and Raman spectroscopy can be used to evaluate the c -axis crystallite size L_c . Fig. 9(c) shows a plot of L_c obtained by X-ray diffraction for the four samples in Fig. 9(a) as a function of the parameter R from Raman spectroscopy. Again an empirical formula was extracted from this

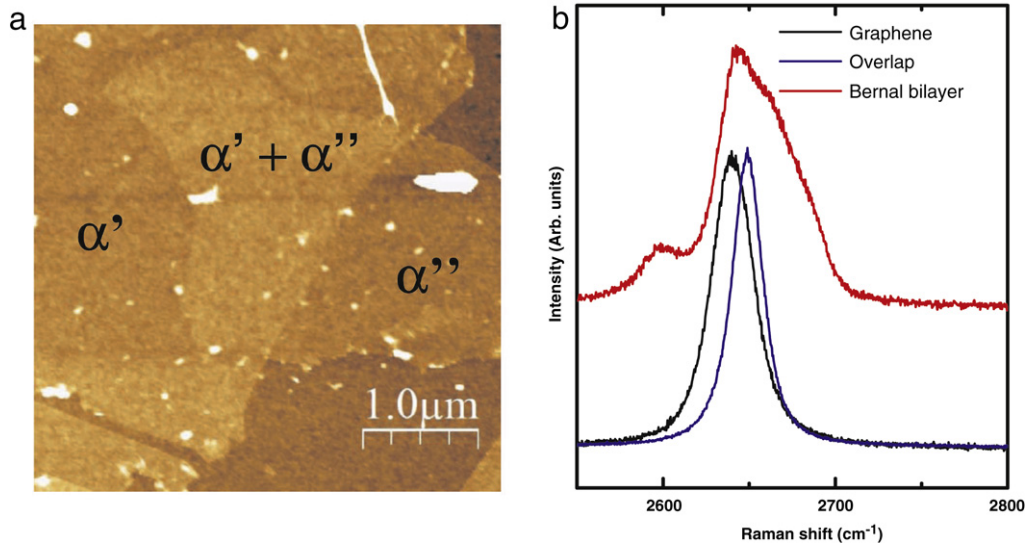


Fig. 10. (a) AFM topographic image of two graphenes (α' and α''), with an overlap region between the two ($\alpha' + \alpha''$) showing a misoriented bilayer graphene. (b) Raman spectra of the G' band for the monolayer graphene region (black), an AB Bernal stacked bilayer graphene (red) and the misoriented bilayer graphene (blue). Adapted from Ref. [74].

experiment [71]

$$L_c(\text{nm}) = 10 + \frac{10}{1.05 - R} \quad (6)$$

which relates the average L_c crystallite size to the ratio R in Eq. (4) for laser excitation energies in the visible range.

In graphene systems where stacking disorder can occur, i.e., for epitaxial or CVD grown graphene (see Section 5), this approach can be used in the future to determine the interplanar distance ($c/2$) and interplanar crystalline thickness. Moreover, careful inspection of the G' band lineshape for samples with c -axis stacking disorder can be useful to determine the contributions to this spectral feature from the AB and non-AB stacking order regions of the sample.

Recently, the Raman spectrum of folded graphene [73] (or misoriented bilayer graphene [74]) have been obtained. Fig. 10(a) presents an atomic force microscopy (AFM) image showing two graphenes (α' and α'') with a region in which the two graphenes are randomly overlapped ($\alpha' + \alpha''$). Fig. 10(b) shows the Raman spectra of the G' band of the graphene (black), a Bernal stacked bilayer (red) and the misoriented bilayer (blue) [74]. The Bernal bilayer spectra in Fig. 10(b) clearly shows a lineshape common to the four peak spectrum which comes from the different electron–phonon scattering processes discussed in Section 2.2 for AB stacked 2-LG. However, the misoriented bilayer graphene has completely lost the characteristics of a Bernal bilayer, and now has a G' lineshape more typical of monolayer graphene [73,74]. Theoretical calculations of a non-AB stacked bilayer have also shown that the electronic structure resembles the massless Dirac Fermions in monolayer graphene [75,76]. The single peak observed for the misoriented bilayer in Fig. 10(b) is in agreement with these calculations, where the DR Raman process occurs between two conduction bands along the $\Gamma KMK' \Gamma$ direction (see Sections 1.1 and 1.3). The difference between the monolayer and the misoriented bi-layer G' Raman spectra is the frequency of the peak, which for the misoriented bi-layer is upshifted by 9 cm^{-1} and broadened in linewidth as seen in Fig. 10(b) [74]. Two groups have reported the same G' band frequency upshift for this kind of non-AB bilayer sample [73,74], and have attributed this effect to a reduction of the Fermi velocity [73] or to a change in the phonon dispersion curves [74].

In this section we have shown that stacking disorder can significantly alter the Raman spectra of the G' band in graphite and few-layer graphene. Previous studies of stacking order in graphite have shown that useful information on the stacking order, the out-of-plane lattice parameter and the c -axis crystallite size can be obtained from Raman spectroscopy [71]. Such information can now also be used to understand and characterize graphene samples with stacking disorder.

3. Resonance Raman studies: Probing electrons and phonons

Resonance Raman scattering (RRS) has been widely used to probe the electronic and phonon structures of carbon materials like carbon nanotubes [77], graphite, diamond-like carbon [78] and linear carbon chains [79]. Also the double resonance Raman model and its second order G' band provide rich information about the energy and momentum of the participating electrons and phonons. In this section we review the combination of RRS and DR Raman processes to probe information about phonons and electrons in monolayer and bilayer graphene.

From the double resonance process model (see Section 1.3) we have a set of two coupled quantities, that is, the wavevectors of electrons and phonons and their dispersion relations. From the knowledge of one of these quantities and

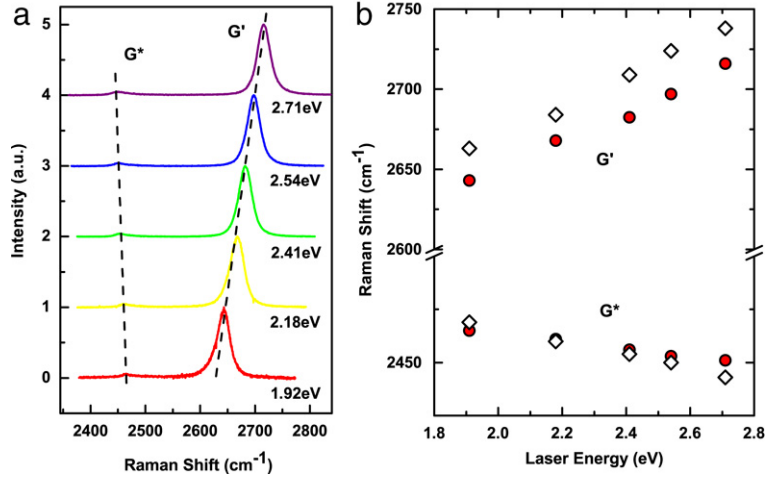


Fig. 11. (a) Raman spectra of the G' and G^* bands of monolayer graphene for 1.92, 2.18, 2.41, 2.54 and 2.71 laser excitation energies. (b) Dependence of $\omega_{G'}$ and ω_{G^*} on laser energy E_{laser} . The circles correspond to the graphene data and the lozenges correspond to turbostratic graphite. Figure from Ref. [52].

information coming from the experimental Raman band originating from a specific double resonance scattering process (for example, the phonon energies and their dispersion), it is possible to get the other quantity (which, for this example, would be information about the electronic structure). By changing the laser excitation energy, different points in momentum space for the electronic and phonon dispersion are probed, and in this way it is possible to map the phonon or electronic dispersion relations by this method. Some basic fundamental concepts related to this method are discussed in Section 1.3.

3.1. Monolayer graphene phonon dispersion

We begin our discussion here with monolayer graphene, which represents the ideal system for calculating the phonon dispersion relations for a variety of carbon structures, and there are several different phonon dispersion models in the literature for describing $\omega(q)$ for graphite and other sp^2 carbons [38,41,80–85]. In many cases, these models contradict each other in terms of the slopes and positions of the phonon branches near the Dirac point (the K point) and this is in part due to the Kohn anomaly [41]. Also different experimental techniques like neutron scattering [86], electron energy-loss spectroscopy [87–89], inelastic x-ray scattering [38,90], and DR Raman scattering [49,62], have been applied to characterize the phonon dispersion. Here, we show that by measuring the Raman spectra of two second-order Raman features with different laser energies, it is possible to obtain experimentally the longitudinal acoustic (LA) and the in-plane transverse optical (iTO) phonon dispersions of monolayer graphene near the Dirac point [52]. We also compare the results thus obtained with the corresponding results for turbostratic graphite and for different phonon dispersion models in the literature.

Figs. 5 and 11(a) shows the Raman spectra in the region of the G^* ($\sim 2450 \text{ cm}^{-1}$) and G' ($\sim 2700 \text{ cm}^{-1}$) bands with different laser excitation energies. As shown in Section 1.3, the G' band comes from an *intervalley* DR Raman process involving an electron with wave vector k in the vicinity of the K point and two iTO phonons with wave vectors $q \approx 2k$, where both k for the electron and q for the phonon are measured from the K point. The G^* band can also be explained by the DR Raman model with an *intervalley* process but involving one iTO and one LA phonon [49] as discussed below.

Fig. 11(b) shows the G' and G^* frequencies as a function of laser energy for graphene and turbostratic graphite. The G' band exhibits a highly dispersive behavior, with a slope of $88 \text{ cm}^{-1}/\text{eV}$ for monolayer graphene and $95 \text{ cm}^{-1}/\text{eV}$ for turbostratic graphite. The G^* band, exhibits a less pronounced dispersion for both materials. In contrast, ω_{G^*} decreases with laser energy by about $-18 \text{ cm}^{-1}/\text{eV}$ for monolayer graphene and by about $-31 \text{ cm}^{-1}/\text{eV}$ for turbostratic graphite [52].

To analyze the experimental data from Fig. 11(b), we first introduce the linear dispersion of a graphene monolayer by noting that the electron energy is given by $E(k) = \hbar v_F k$, where v_F is the Fermi velocity and k is the electron wave vector measured with respect to the K point. Thus the DR Raman conditions are given by:

$$\omega_{\text{laser}} = 2v_F k \quad (7)$$

$$\omega_{\text{ph}} = v_F(k - k') \quad (8)$$

$$q = k + k' \quad (9)$$

where ω_{laser} and ω_{ph} are the laser and phonon frequencies and k' is the scattered electron wave vector near the K' point.

From the measured frequencies ω_{G^*} and $\omega_{G'}$ shown in Fig. 11, we can obtain the experimental values for the LA and iTO phonons near the Dirac point. The iTO frequency can be obtained from $\omega_{G'}/2$, and the LA frequency (ω_{LA}) is obtained from

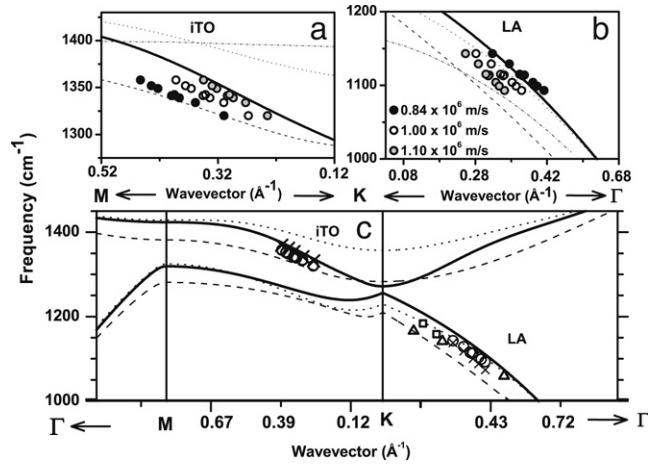


Fig. 12. (a) Experimental data obtained from the DR scattering process for the (a) iTO phonons and (b) the LA phonons in monolayer graphene, considering three different values for the Fermi velocity v_F , and theoretical phonon dispersion models by Maultzsch et al. [38] (dashed curves), Dubay et al. [83] (dotted curves), Popov and Lambin [85] (continuous curves) and Benedek and Onida [81] (dash dotted curve). (c) Experimental phonon frequencies obtained from DR Raman scattering for graphene (circles) and turbostratic graphite (crosses) and inelastic X-ray scattering data by Maultzsch et al. [38] (triangles) and Mohr et al. [90] (squares). Figure from Ref. [52].

subtracting the iTO frequency from the G^* band frequency:

$$\omega_{\text{iTO}}(q) = \omega_{G'}(q)/2 \quad (10)$$

$$\omega_{\text{LA}}(q) = \omega_{G^*}(q) - \omega_{G'}(q)/2 \quad (11)$$

So, using Eqs. (7)–(9) we obtain the phonon wave vector q observed for each laser energy and, with the results of Eqs. (10) and (11), the dispersion of ω_{LA} and ω_{iTO} phonons can be plotted.

As discussed above, we can only determine the phonon velocities in a double resonance Raman experiment as a function of the Fermi velocity v_F for the electrons near the Dirac point. In order to plot experimental results [52] for the phonon dispersion relation, we need to consider a specific value for the Fermi velocity. Fig. 12 shows experimental data [52] for ω_{iTO} [Fig. 12(a)] and ω_{LA} [Fig. 12(b)] for monolayer graphene as a function of the phonon wave vector q considering three different values of v_F : 0.84×10^6 m/s (black circles), 1.0×10^6 m/s (white circles), and 1.1×10^6 m/s (gray circles), which correspond to the values of the nearest-neighbor tight-binding overlap energy γ_0 of 2.6, 3.1 and 3.4 eV, respectively [51]. Four different phonon dispersion models are also shown in Fig. 12 for the iTO and the LA branches. These models correspond to the first-principles calculations by Maultzsch et al. [38] (dashed curves) and Dubay et al. [83] (dotted curves), the force constant model by Popov and Lambin [85] (continuous curves) and the bond charge model reported by Benedek and Onida [81] (dash dotted curve). The best agreement between the experimental and theoretical data is given when we consider a Fermi velocity of 1.0×10^6 m/s and the theoretical model for the iTO phonon dispersion by Popov and Lambin [85], which nicely describes the Kohn anomaly as observed experimentally. Fig. 12(c) shows the phonon dispersion curve around the K point with $v_F = 1.0 \times 10^6$ m/s, comparing the different phonon models, as well as with the measured results for turbostratic graphite and with different experimental inelastic X-ray scattering data for graphite [38,52].

Another important quantity that can be extracted using this approach is the phonon velocity for both phonon branches (v_{iTO} and v_{LA}). By deriving ω_{ph} with respect to q and considering the DR conditions shown in Eqs. (7)–(9), we obtain the following expressions that relate the phonon velocities with the Fermi velocity v_F for electrons:

$$v_{\text{iTO}} = (d\omega_{G'}/d\omega_{\text{laser}})v_F/2 \quad (12)$$

$$v_{\text{LA}} = \left(d\omega_{G^*}/d\omega_{\text{laser}} - \frac{1}{2}d\omega_{G'}/d\omega_{\text{laser}} \right) v_F. \quad (13)$$

By using the experimental laser frequency ω_{laser} , the dependence of ω_{G^*} and $\omega_{G'}$ on E_{laser} shown in Fig. 11(b), the following values are obtained for the LA and iTO velocities near the Dirac point of monolayer graphene: $v_{\text{LA}} = 7.70 \times 10^{-3}v_F$ and $v_{\text{iTO}} = 5.47 \times 10^{-3}v_F$. The corresponding values found for turbostratic graphite are: $v_{\text{LA}} = 9.82 \times 10^{-3}v_F$ and $v_{\text{iTO}} = 5.96 \times 10^{-3}v_F$ [52], using $v_F = 1.0 \times 10^6$ m/s, consistent with the value given above for graphene.

3.2. Bilayer graphene phonon and electronic structure

We now turn to the electronic properties of bilayer graphene as probed by RRS. Bilayer graphene has a richer G' band spectrum, because of its special electronic structure consisting of two conduction and two valence bands (see Fig. 6). From

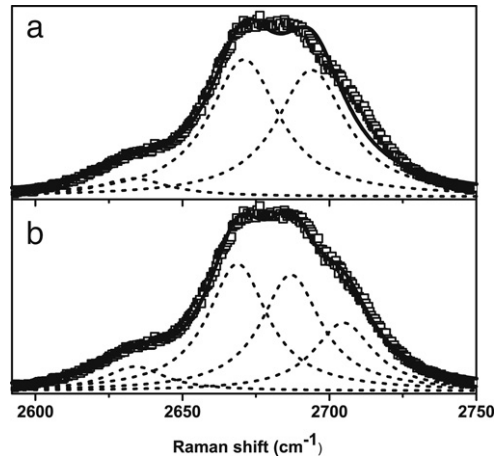


Fig. 13. Fitting the measured spectra of the G' band for bilayer graphene at 2.18 eV laser excitation energy with (a) three Lorentzians with an FWHM of 29 cm^{-1} [55] and with (b) four Lorentzians with an FWHM of 24 cm^{-1} [91].

the DR Raman process in bilayer graphene, it is possible to distinguish four Lorentzians in the experimental Raman spectra for each laser line [20]. Fig. 13(a) and (b) compares a G' -band spectrum recorded with 2.18 eV laser energy, where the fitting was done with three and four Lorentzians. The rationale for using three Lorentzians to fit the G' -band spectrum for bilayer graphene comes from the mirror band approximation relative to the Fermi energy commonly used to describe the linear $E(k)$ relation in graphene. Using this approximation, Park et al. calculated the matrix elements contributing to the transitions in Fig. 6 [55], assuming a degeneracy of the P_{12} and P_{21} transition energies consistent with the mirror band model. The experimental results in Fig. 13(a) show two important points. First, it is seen that the FWHM for the three peak fit to the data is increased to 29 cm^{-1} , which is larger than that in monolayer graphene, 24 cm^{-1} , and second, the fit of the experimental data to three Lorentzians is not satisfactory [55]. The experimental data in Fig. 13(b) [63] taken at 2.18 eV clearly show the need for four peaks to describe the G' band of bilayer graphene, as discussed in Section 2.2. These experimental results [63] provide clear experimental evidence for an asymmetry between the valence and conduction bands.

By fitting the G' band spectrum for each one of the laser energies with four Lorentzians with a FWHM of 24 cm^{-1} , we can plot the position of each peak as a function of laser energy. Fig. 14 shows the dispersion of each one of the four peaks that comprise the G' band as a function of laser energy. Each one of the DR Raman processes that gives rise to one of the G' peaks is labeled as P_{ij} ($i, j = 1, 2$), in Fig. 14 and the related process is depicted in Fig. 6(a)–(d). Since the iTO phonon along the KM direction increases its frequency with increasing wave vector q , the highest frequency of the G' peak for a given E_{laser} energy is associated with the P_{11} process, which has the largest wave vector (q_{11}). The smallest wave vector q_{22} is associated with the process P_{22} , which gives rise to the lowest frequency peak of the G' band. The two intermediate peaks of the G' band are associated with processes P_{12} and P_{21} [63].

Now we apply the DR Raman model to relate the electronic and phonon dispersion of bilayer graphene with the experimental dependence of the G' band peaks energy as a function of laser energy. According to the DR Raman process for bilayer graphene (see Section 1.3 and Fig. 6) an electron in a P_{ij} process with wave vector k_i is resonantly excited from the valence band π_i to the conduction band π_i^* by absorbing a photon with energy E_{laser} . This electron is then resonantly scattered to a state with wave vector k'_j by emitting a phonon with momentum q_{ij} and energy E_p^{ij} . Finally, the electron is scattered back to state k_i by emitting a second phonon, and it recombines with a hole producing a scattered photon with an energy $E_s = E_{\text{laser}} - 2E_p^{ij}$. The phonon wave vector q_{ij} , measured from the K point and along the KM direction, is given by $q_{ij} = k_i + k'_j$. As discussed in Section 2.2, the P_{11} and P_{22} processes are related to a phonon with T_1 symmetry and the other two processes to a phonon with T_2 phonon symmetry.

The electronic structure of bilayer graphene can be described by the phenomenological Slonczewski-Weiss-McClure (SWM) model [5,65,66]. Since the number of atoms in the unit cell of bilayer graphene with the Bernal AB stacking structure is the same as the unit cell for graphite which has the same stacking structure, we can denote the electronic spectrum of bilayer graphene in terms of a model closely related to the SWM model for graphite, by determining the parameters γ_0 , γ_1 , γ_3 and γ_4 , that are associated with overlap and transfer integrals calculated for nearest neighbors atoms. The pairs of atoms associated with these parameters are indicated in the atomic structure of bilayer graphene shown in Fig. 15. Along the K – Γ direction we can replace σ by $\gamma_0 [2 \cos(2\pi/3 - ka_{c-c}\sqrt{3}/2) + 1]$ in McClure's expressions [5]. Here k is measured from the K point and $a_{c-c} = 0.142 \text{ nm}$ is the in-plane nearest neighbor carbon distance. Since there is no k_z -dependence we may set the following parameters in McClure's expressions at $\Gamma = 1$ and $\gamma_2 = \gamma_5 = 0$ (γ_2 and γ_5 correspond to 3rd layer interactions in graphite). Also the parameter Δ is weaker for describing the G' dispersion in graphite and should by symmetry be zero for bilayer graphene [68]. With these simplifications to adopting the McClure model [65,66], the electronic bands in bilayer

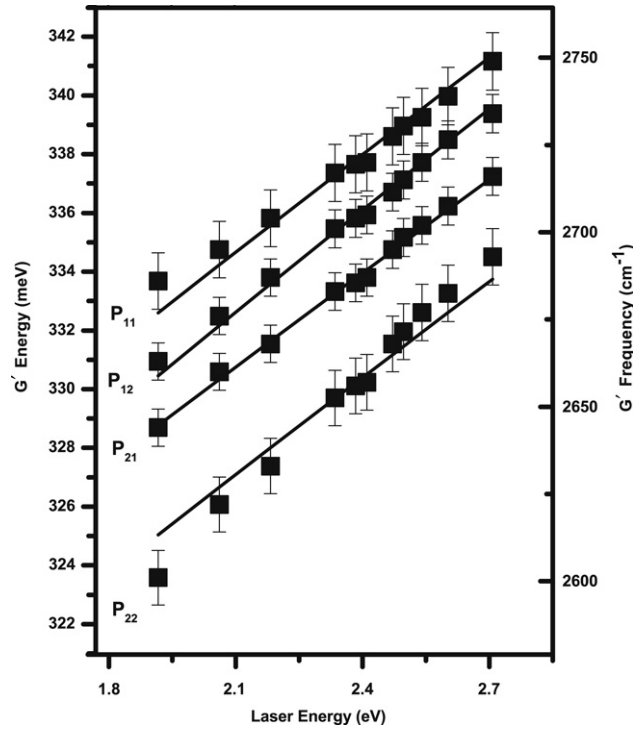


Fig. 14. The position of the four peaks that comprise the G' band of bilayer graphene as a function of laser energy (E_{laser}) [63].

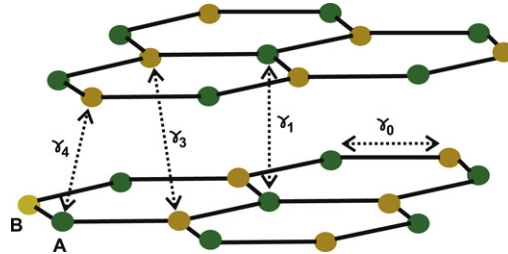


Fig. 15. Atomic structure of bilayer graphene, where the overlap γ parameters are shown with the respective pair of atoms appropriate for each γ_i interaction [63].

graphene can be described as [63,67]:

$$E_{\pi_2} = (-\gamma_1 - v_3\sigma - \xi_+)/2, \quad (14)$$

$$E_{\pi_1} = (\gamma_1 + v_3\sigma - \xi_-)/2, \quad (15)$$

$$E_{\pi_1^*} = (-\gamma_1 - v_3\sigma + \xi_+)/2, \quad (16)$$

$$E_{\pi_2^*} = (\gamma_1 + v_3\sigma + \xi_-)/2, \quad (17)$$

where

$$\xi_{\pm} = \sqrt{(\gamma_1 - v_3\sigma)^2 + 4(1 \pm v_4)^2\sigma^2}, \quad (18)$$

and $v_j \equiv \gamma_j/\gamma_0$.

Applying the DR Raman conditions we have:

$$E_{\text{laser}} = E_{\pi_i^*}(k_i) - E_{\pi_i}(k_i) \quad (19)$$

$$E_p^{ij}(k_i + k'_j) = E_{\pi_i^*}(k_i) - E_{\pi_j^*}(k'_j). \quad (20)$$

Eq. (16) determines the initial k_i electron wave vector as a function of the band parameters. Assuming that the iTO phonon dispersion is linear in the measured energy range, we have $E_p^{ij}(k_i + k'_j) = [A + B(k_i + k'_j)]$. Then Eq. (20)

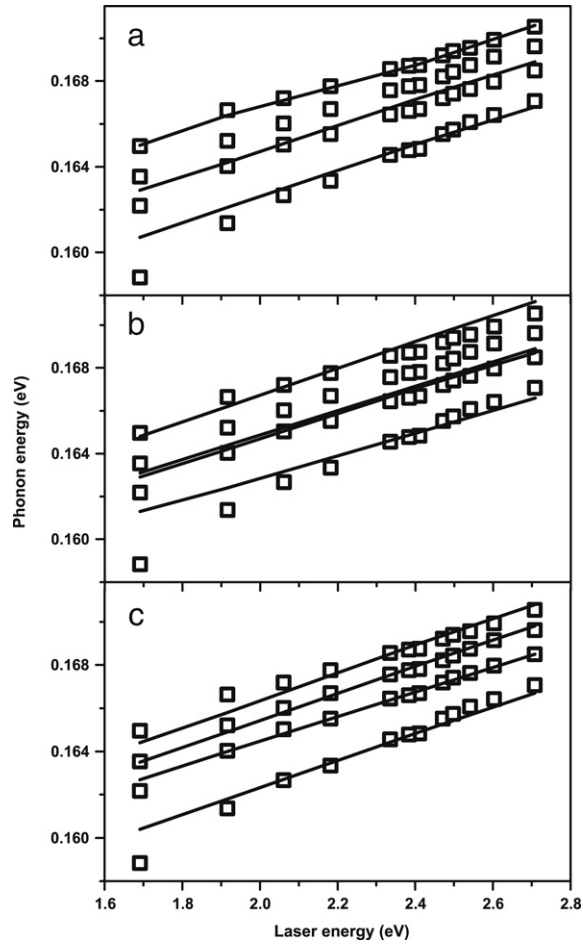


Fig. 16. Experimental phonon energies (open squares) derived from the G' band for bilayer graphene as a function of laser excitation energy and the fitted curves (full lines) from Ref. [56] using (a) $\gamma_3 = \gamma_4 = 0$, (b) $\gamma_3 \neq 0$ and $\gamma_4 = 0$ and (c) $\gamma_3 \neq 0$ and $\gamma_4 \neq 0$ (see Table 6).

Table 6

Experimental SWM parameters (in eV) for the electronic band structure of bilayer graphene from Fig. 14. The parameters for graphite are taken from Refs. [5,92] for a sample for which $\varepsilon_F = -0.024$ eV.

	γ_0	γ_1	γ_2	γ_3	γ_4	γ_5	$\gamma_6 = \Delta$
Bilayer graphene	2.9	0.30	n/a	0.10	0.12	n/a	n/a
Graphite	3.16	0.39	-0.02	0.315	0.044	0.038	-0.008

uniquely determines the scattered k'_j electron wave vector, and $E_p^{ij}(k_i + k'_j)$ can be computed for each one of the P_{ij} processes for each laser excitation energy. By making a least squares fit of the experimental data to the above equations, it is possible to find the best set of electronic and phonon parameters that fit the experimental data. Fig. 14 shows the experimental data (symbols) in comparison with the theoretical model (solid lines) [63]. Fig. 16 also compares the SWM model (Slonzewski–Weiss–McClure) [5,65,66], including (a) only γ_0 and γ_1 , (b) only γ_0 , γ_1 and γ_3 and (c) all γ_0 , γ_1 , γ_3 and γ_4 parameters [63,91]. When $\gamma_3 = \gamma_4 = 0$, the two inner DR Raman processes become degenerate [Fig. 16(a)], corresponding to mirror valence and conduction bands. By setting $\gamma_3 \neq 0$ and $\gamma_4 = 0$ [Fig. 16(b)], the trigonal warping effect [5] is included and the degeneracy found in Fig. 16(a) is broken, but the calculated energy separation for the P_{12} and P_{21} is still too small to account for the experimental observations. In Fig. 16(c) where $\gamma_3 \neq 0$ and $\gamma_4 \neq 0$, the fit with the experimental data is successful. The γ_4 in the SWM model is responsible for the difference between the electron and hole effective masses [5]. Therefore, the P_{12} and P_{21} processes are associated with phonons with different momenta that participate in these scattering mechanisms revealing an electron–hole asymmetry in bilayer graphene. Table 6 summarizes the tight binding γ values for bilayer graphene, as compared with the graphite values in the literature [63]. Also the results for the two linear phonon dispersions found in the fitting procedure are shown in Table 7 [63].

In this section we summarized how the combination of the RRS experimental data and the DR Raman model can give important knowledge about the electronic and phonon structure in graphene materials. For monolayer graphene [52], the

Table 7

Values obtained for the G' band phonon dispersion for bilayer graphene from Fig. 14 for the two iTO phonon branches of bilayer graphene near the K point, where $E_p^{ii} = A_{ii} + B_{ii}q$ corresponds to the P_{11} and P_{22} processes and $E_p^{ij} = A_{ij} + B_{ij}q$ to the P_{12} and P_{21} processes.

A_{ii}	B_{ii}	A_{ij}	B_{ij}
153.7 (meV)	38.5 (meV Å)	154.0 (meV)	38.8 (meV Å)
1238 (cm ⁻¹)	310 (cm ⁻¹ Å)	1241 (cm ⁻¹)	313 (cm ⁻¹ Å)

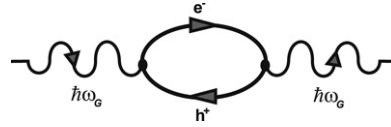


Fig. 17. Feynman diagram for the second-order process that renormalizes the phonon energy. The first node shows the decay of a G -band phonon into an electron–hole pair, and the second node shows the recombination of the electron and hole resulting in the emission of a phonon.

phonon structure of the iTO and LA phonon modes near the Dirac point were probed by the use of the selection rules of the DR Raman process in combination with different laser excitation energies. For bilayer graphene [63], using a tight binding model related to graphite, the corresponding band parameters were obtained and the results reveal electron–hole asymmetry. The comparison of 2-LG to graphite is not expected to yield the same band parameters because the unit cell for bilayer graphene has empty space bounding the exteriors of the upper and lower layers while graphite has similar unit cells, to form a 3D lattice of these unit cells. The graphite structure has a k_z dependence of the dispersion relations, which is absent in bilayer graphene. The departure of the data points for the P_{22} transition from the linear fit at $E_{\text{laser}} < 2.4$ eV is due to the non-linear phonon dispersion that occurs near the Dirac point.

4. Raman studies on gated graphenes: Electron–phonon interaction

4.1. Interaction of phonons with electron–hole pairs: Theoretical background

4.1.1. Monolayer graphene

The interaction between electrons and phonons is a fundamental issue for understanding many of the physical properties of graphenes, such as electronic transport, excited electron relaxation and thermal conductivity. Since graphene is a zero-gap semiconductor, the lattice vibrations are partially screened by the conduction electrons. In 1959, Kohn [40] showed that this screening changes rapidly as a function of wave vector \mathbf{q} for phonons with special \mathbf{q} -vectors, giving rise to a divergence in the phonon dispersion $\omega(\mathbf{q})$ at these special points. This effect is known as the Kohn anomaly, and it occurs for a vector \mathbf{q} satisfying the condition $\mathbf{q} = \mathbf{k}_1 - \mathbf{k}_2 + \mathbf{b}$, where \mathbf{k}_1 and \mathbf{k}_2 are wavevectors of the electron states at the Fermi level, and \mathbf{b} is a reciprocal lattice vector, necessary to bring the phonon wavevector \mathbf{q} into the 1st Brillouin zone.

In the case of graphene, the Fermi wavevectors \mathbf{k}_1 and \mathbf{k}_2 correspond to the corners of the 1st Brillouin zone (namely the \mathbf{K} and \mathbf{K}' vectors; see Fig. 1(e)) and, as first reported by Piscanec et al. [41], the Kohn anomaly occurs for special phonons at the Γ and K points of graphene. The phonon branches exhibiting the Kohn anomaly at the Γ and K points are those associated with the Raman G -band and G' -band, respectively [41]. In particular, it was shown in this work [41] that the slopes of the phonon dispersion at these special points are proportional to the electron–phonon coupling parameter λ_{e-p} .

The physical origin for the Kohn anomaly in graphene is explained by the special mechanism illustrated in Fig. 17, in which an electron in the valence band is first excited to the conduction band by absorbing a phonon, thus creating an electron–hole pair. The electron and hole then recombine, thus emitting a phonon. Both the frequency and lifetime of the phonon are significantly affected by this second-order process [93–95]. The renormalization of the phonon energy can be described by time dependent second-order perturbation theory, in which the contribution to the energy of the electron–hole bubble process depicted in Fig. 17 is negative, giving rise to a softening of the phonon energy with respect to the unperturbed phonon energy.

The renormalization of the phonon energy is also strongly dependent on the Fermi level position, so that it can be tuned by doping graphene with electrons or holes. In fact, if one changes the Fermi energy of the system, there is a reduction in the interaction between phonons and interband electron–hole pairs, thus changing the effective force constant of these atomic vibrations. This renormalization, which is very effective when $E_F = 0$ (the Fermi level at the Dirac point in monolayer graphene), is inhibited when the change in the Fermi level is larger than half of the G -band phonon energy since, as shown in Fig. 18, the Pauli exclusion principle in this case suppresses the process depicted in Fig. 17 (creation of an electron–hole pair by exciting a phonon).

Theoretical models for the phonon self-energy [93–95] have predicted a logarithmic dependence of the phonon softening on chemical potential (or Fermi level change) when it is smaller than half of the phonon energy, and a negative singularity when it is exactly half of the phonon energy. However, the logarithmic softening and the negative singularity can be smoothed out by the presence of imperfections in the sample or by temperature effects. Parallel with the dependence of

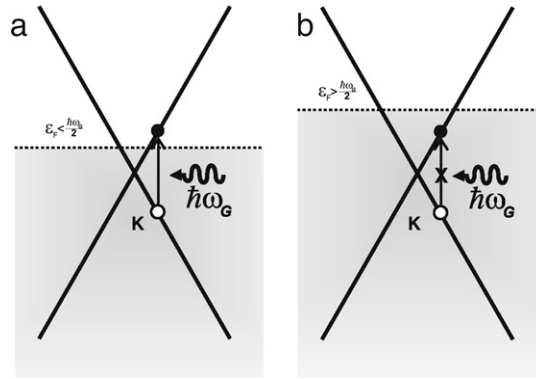


Fig. 18. The renormalization of the phonon energy, associated with the mechanism shown in Fig. 17, is allowed when the change in the Fermi energy $\Delta\epsilon_F$ is smaller than half of the phonon energy $\hbar\omega_G/2$ (left figure) and it is suppressed for $\Delta\epsilon_F > \hbar\omega_G/2$ (right figure).

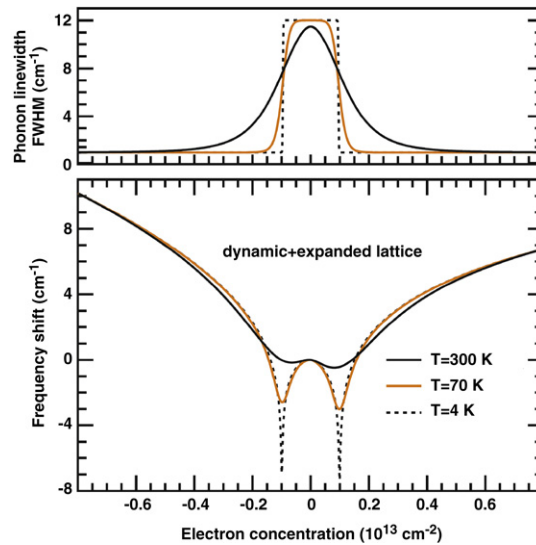


Fig. 19. Linewidth and Frequency of the Raman G band as a function of the electron concentration which is proportional to the square of the Fermi level energy. Adapted from Ref. [96].

the phonon energy on the chemical potential, an increase in the phonon lifetime is predicted by moving the Fermi level position away from the Dirac point, since the phonon decay into electron–hole pairs is inhibited, as shown in Fig. 18.

Fig. 19 shows a theoretical calculation of both the phonon energy and linewidth as a function of the electron concentration, performed by Lazzeri and Mauri [96] at three different temperatures. It is important to emphasize that this calculation was performed by considering a non-adiabatic process, which is a necessary condition due to the very strong electron–phonon interaction in graphene. Notice that the logarithm divergence of the phonon frequency shown in Fig. 19, which is very pronounced at low temperature, is smoothed out at room temperature. The phonon linewidth dependence, which exhibits a barrier-like behavior at low temperature, is also smoothed out at room temperature. So, by moving the Fermi level from the Dirac (neutrality) point, we expect mostly a hardening of the phonon energy and a narrowing of the phonon linewidth.

4.1.2. Bilayer graphene

In the case of bilayer graphene, the E_{2g} phonon mode splits into two components, associated with the symmetric (S) and anti-symmetric (AS) displacements of the atoms in the two layers. Moreover, due to the splitting of the π and π^* bands in this material, phonons can couple with electron–hole pairs produced by interband or intraband transitions. In the case of *interband* transitions, the electron is in the conduction band and the hole is in the valence band, whereas for *intraband* transitions both the electron and the hole are either in the valence band or the conduction band. Ando [97] recently calculated the self-energy of the S and AS phonons for varying Fermi energies and predicted a hardening and softening of the S and AS phonons, respectively, induced by electron or hole doping.

In order to discuss the phonon renormalization effect in bilayer graphene, we must consider the selection rules for the interaction of the symmetric S and anti-symmetric AS phonons with the interband or intraband electron–hole pairs. The

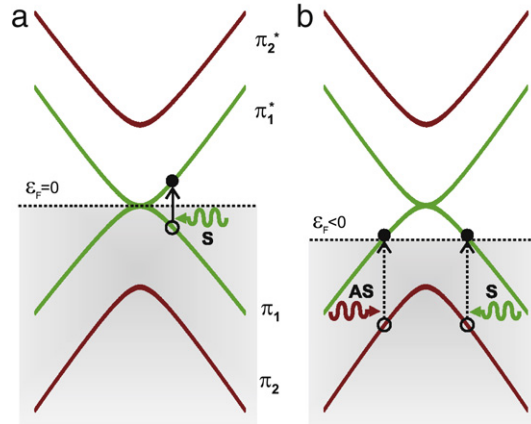


Fig. 20. (color online) Parabolic band structure of bilayer graphene near the K point. The vertical arrows illustrate the possible transitions induced by symmetric (green) and antisymmetric (red) $\mathbf{q} = 0$ phonons for (a) interband electron–hole pair creation when $\varepsilon_F = 0$ and (b) intraband electron–hole pair creation when $\varepsilon_F < 0$. The opening of an energy gap around the Dirac point is not considered in this diagram.

band structure of bilayer graphene near the K point shown in Fig. 20 consists of four parabolic bands, two of which touch each other at the K point, while the other two bands are separated by $2\gamma_1$, where $\gamma_1 \sim 0.35$ eV.

The electron–phonon interaction in bilayer graphene is described by a 2×2 matrix for each phonon symmetry, where each matrix element gives the contribution of electron–hole pairs involving different electronic sub-bands [97]. For the symmetric phonon mode, all matrix elements are different from zero, and this phonon can interact with both interband or intraband electron–hole pairs, as shown in Fig. 20(a), giving rise to the phonon energy renormalization (Kohn anomaly). However, for the anti-symmetric phonon mode, the diagonal terms of the matrix vanish, showing that there is no coupling between the AS phonons and interband electron–hole pairs. Therefore, no Kohn anomaly is expected for the antisymmetric phonon mode when the Fermi level is at the Dirac point.

However, if the Fermi energy is moved either up or down with respect to the Dirac point, [for instance, $\varepsilon_F < 0$ as shown in Fig. 20(b)], then intraband electron–hole pairs can be produced by phonons. In this case, the anti-symmetric phonons also have their energies renormalized, giving rise to the Kohn anomaly.

4.2. Experimental results

4.2.1. Monolayer graphene

As discussed in the previous section, the coupling between phonons and electron–hole pairs renormalizes the phonon energy of graphene, and the renormalization depends on the electron and hole concentrations. The effect is strong near the Γ and K points in the Brillouin zone. Thus phonons that are important for this process are those with $\mathbf{q} = 0$ and for $\mathbf{q} = \mathbf{K}$, where \mathbf{K} denotes the Brillouin zone corner of graphene (see Fig. 1(e)). The zone center E_{2g} phonon mode of graphene, which gives rise to the Raman G -band, is known to exhibit a very strong coupling with electron–hole pairs. This effect can be measured directly by Raman spectroscopy, as it probes the G band frequency as a function of Fermi energy.

The modification of the Fermi level of graphenes can be done by electrochemical methods [98] or by an electric field effect when a gate voltage is applied between the Si substrate and the graphene, deposited on the top of a Si/SiO₂ substrate [99,100]. Recent Raman studies of monolayer graphene have shown that the modification of the Fermi level induces changes in the frequency and width of the G -band, appearing in Raman spectra around 1580 cm^{-1} , and these changes are ascribed to the dependence of the electron–phonon process depicted in Fig. 17 on the Fermi level position.

Fig. 21 shows the Fermi energy dependence of the frequency and width of the Raman G -band in monolayer graphene, as measured by Yan et al. [100]. A similar result was reported by Pisana et al. [99]. The G -band frequency of monolayer graphene increases and the G -band linewidth decreases when the Fermi level is moved away from the Dirac point, due to doping by either electrons or holes (positive or negative changes in the Fermi level). The logarithmic phonon softening, predicted theoretically when the chemical potential is smaller than half of the phonon energy, has not yet been observed in monolayer graphene samples, possibly due to the presence of non-uniformity in the spatial distribution of the charge density in presently available monolayer graphene samples.

4.2.2. Bilayer graphene

Recently, Yan et al. [101] reported a low temperature (12 K) Raman investigation of a bilayer graphene sample where the charge density was modulated by an electric field, and they observed a logarithmic softening of the G -band frequency by about 1 cm^{-1} for changes in the Fermi level smaller than half of the phonon energy similar to the predictions of Fig. 19. This observation was ascribed to both the large density of states and the lesser importance of the charge density inhomogeneity in the large density of states of bilayer graphene at the Dirac point as compared to monolayer graphene.

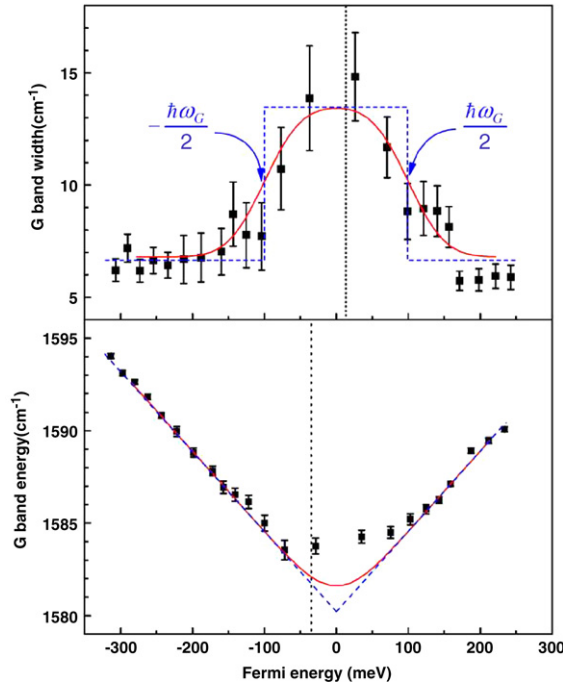


Fig. 21. G band FWHM linewidth (upper figure) and energy (lower figure) of monolayer graphene, as a function of the Fermi level energy. Adapted from Ref. [100].

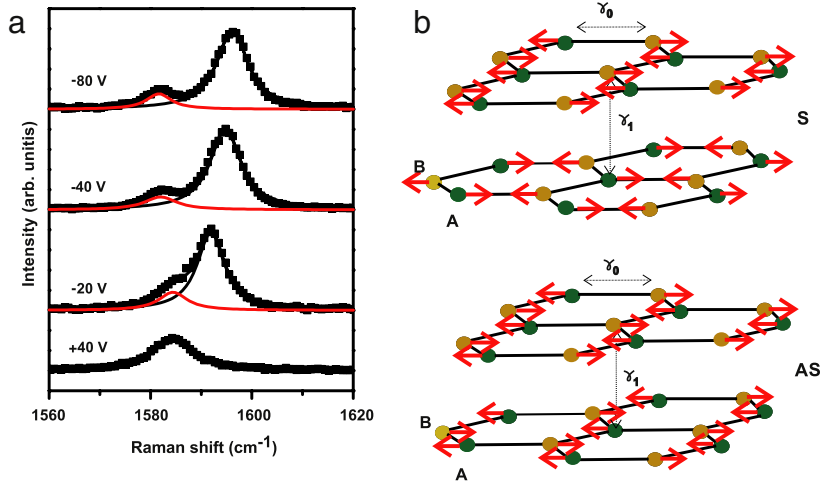


Fig. 22. (color online) (a) Raman G-band of the bilayer graphene for -80 V, -40 V, -20 V and $+40$ V gate voltages. Two Lorentzian curves are needed to fit the G-band for -80 V, -40 V and -20 V and a single Lorentzian for $+40$ V. (b) Displacement of the carbon atoms for the symmetric (S) and anti-symmetric (A) highest energy phonon modes at the Γ point of bilayer graphene [102].

Malard et al. [102] reported a Raman study of back-gated bilayer graphene samples, and showed that the G-band of a bilayer graphene sample for negative gate voltage is clearly composed of two components which show an opposite behavior upon changing the Fermi level (see Fig. 22(a)).

Fig. 23(a) and (b) show, respectively, the relative shift $\Delta\omega_G$ (with respect to the G-band position in the $+50$ V spectrum) and the full width at half maximum (FWHM) intensity of the Lorentzians that fit the G-band lineshapes as a function of the applied gate voltage. Notice that the frequency of the high energy component increases with decreasing values of V_g , whereas the opposite behavior is observed for the low energy component. Fig. 23(b) shows that the FWHM exhibits a maximum for the $V_g = +50$ V spectrum, and it clearly decreases with more negative values of V_g . The absence of an initial softening of the G-band for $|\varepsilon_F| < \hbar\omega_G/2$ can be explained by the presence of a large inhomogeneous spatial charge distribution in the sample and by the fact that this experiment was done at room temperature.

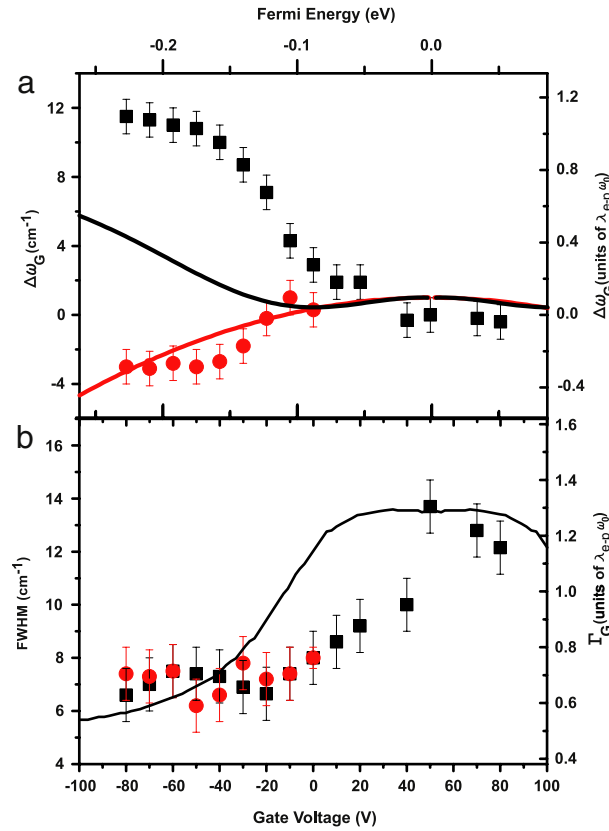


Fig. 23. (color online) (a) The black squares and red circles correspond, respectively, to the relative shifts ($\Delta\omega_G$) of the symmetric (+) and anti-symmetric (–) components of the G band, with respect to the position in the +50 V spectrum, as a function of the applied gate voltage V_g (bottom scale) [102]. The solid curves correspond to the theoretical prediction for the relative G-band shift $\Delta\omega_G^{(\pm)}$ [97] in units of $\lambda_{e-p}\omega_0$ as a function of the Fermi energy ε_F (top scale). (b) The black squares and red circles correspond, respectively, to the FWHM linewidth Γ_G of the symmetric and anti-symmetric components of the G-band, and the solid curve corresponds to the theoretical predictions for the symmetric phonon mode [97]. $V_g = +50$ V corresponds experimentally to the Dirac point which is denoted by $\varepsilon_F = 0$ in the theoretical solid curves, suitably translated.

Bilayer graphene is formed by two graphene layers with AB Bernal stacking, where the group of the wave vector at the Γ point is D_{3d} (see Section 1.4). The phonon branch associated with the E_{2g} mode of monolayer graphene gives rise to two branches for bilayer graphene (one S and the other A), with in-phase and out-of-phase displacements of the atoms in the two layers, which are represented at Fig. 22(b). At the center of the Brillouin zone (Γ point), the symmetric and anti-symmetric vibrations belong to the two doubly degenerate representation E_g and E_u , respectively. The anti-symmetric (odd parity) E_u mode is not Raman active, since the D_{3d} group is centro-symmetric. However, if the inversion symmetry operation of bilayer graphene is broken, the group of the wave vector is then described by the C_{3v} point group at the Γ point. In this case, both the symmetric and the anti-symmetric modes belong to the E representation, and both are Raman active (see Section 1.4). The breaking of inversion symmetry can be due to the different materials that the top and bottom graphene layers of the device are exposed to and/or to an inhomogeneous doping of the top and bottom graphene layers. The non-equivalence between the top and bottom layers lowers the symmetry, making the anti-symmetric mode active in the Raman spectra, thereby explaining the appearance of two components in the Raman G-band.

Fig. 23(a) and (b) also show a frequency shift $\Delta\omega_G$ and an FWHM broadening (Γ_G) of the G band, as calculated by Ando [97] in terms of $\Delta\omega_G = \text{Re}[\pi^{(\pm)}(\omega)]$ and $\Gamma_G = -2\text{Im}[\pi^{(\pm)}(\omega)]$ [103], respectively, where $\pi^{(\pm)}$ is the phonon self energy for the symmetric (+) and anti-symmetric (–) components as a function of frequency ω , as described in Ref. [97]. The phenomenological damping parameter δ in the phonon self-energy expression [97] describes the charge inhomogeneity in the sample that smooths out the logarithmic singularity which is expected to occur at $\varepsilon_F = \hbar\omega_0/2$. The value of $\delta = 0.1$ eV was considered in the theoretical curves depicted in Fig. 23, since this is the smallest value of δ necessary to remove phonon softening for $\varepsilon_F < \hbar\omega_0/2$ [97,104].

Theoretical curves for $\Delta\omega_G$ and Γ_G are calculated in units of λ_{e-p} , where $\omega_0 = 0.196$ eV is the energy of the optical phonon and λ_{e-p} is related to the strength of the electron–phonon coupling given by [97,105]:

$$\lambda_{e-p} = 0.16 \times 10^{-3} (\text{\AA}^2 \text{ eV}^{-2}) \left[\frac{\partial \gamma_0}{\partial b} \right]^2 \quad (21)$$

where γ_0 is the in-plane nearest-neighbor tight-binding parameter [see Fig. 22(b)] and b is the nearest neighbor C–C distance with an equilibrium value of $a_{C-C} = 0.142$ nm.

In order to compare the experimental and theoretical results depicted in Fig. 23(a) and (b) we need to convert the experimental horizontal scale (applied gate voltage, in the bottom axis of Fig. 23) into the theoretical scale (Fermi energy, in the upper axis of Fig. 23), and the experimental vertical scales (in cm^{-1} , left side axes of Fig. 23) into the theoretical scales (in units of $\lambda_{e-p}\omega_0$, right side axes of Fig. 23).

To match the scales of the experimental (left axis) and calculated (right axis) values of $\Delta\omega_G$ and Γ_G , shown in Fig. 23, the value $\partial\gamma_0/\partial b = 6.4 \text{ eV \AA}^{-1}$ was used in Eq. (21) [95]. Both of the theoretical curves, for $\Delta\omega_G$ and Γ_G , are plotted in Fig. 23 as a function of the Fermi energy ε_F (top axis), while the experimental values are plotted as a function of gate voltage (bottom axis). In order to scale these axes, we need to consider that both ε_F and V_g are related to the electron (or hole) density n , which is assumed to be the same in both layers. The absolute value of the Fermi energy $|\varepsilon_F|$ is related to the electron (or hole) carrier density in the regime $|\varepsilon_F| < \gamma_1$ by [97]:

$$|\varepsilon_F| = \frac{1}{2} \left(-\gamma_1 + \sqrt{4n\pi\gamma^2 + \gamma_1^2} \right), \quad (22)$$

where $\gamma = \sqrt{3}/2a\gamma_0$, $a = 0.246$ nm is the lattice constant, $\gamma_0 \approx 3$ eV (the in-plane nearest neighbor overlap energy) and $\gamma_1 \sim 0.35$ eV is the out-of-plane nearest-neighbor overlap energy parameter [see Fig. 23(b)]. A parallel plate capacitor model gives $n = 7.2 \times 10^{10} \text{ cm}^{-2}\text{V}^{-1}(V_g - V_D)$, where V_D is the gate voltage needed to move the Fermi level to the Dirac point due to the intrinsic doping of the sample. The value of $V_D = +50$ V was obtained from the experimental spectrum as the gate voltage where the G-band has the largest FWHM linewidth [see lower figure in Fig. 21], since the symmetric phonon lifetime is a minimum for $\varepsilon_F = 0$ (at the Dirac point) [97].

Fig. 23 shows that there is a qualitative agreement between the experimental results and the theoretical prediction of the Fermi level dependence of the frequency and the width of the symmetric and anti-symmetric optical phonon modes in bilayer graphene. The hardening of the symmetric mode and the softening of the antisymmetric phonon mode when the sample is doped is explained by the selection rules associated with the creation of interband or intraband electron–hole pairs by symmetric and anti-symmetric optical phonons [102]. Some of the difference between the experimental results and the theoretical predictions may be related to the different carrier densities in the lower and upper graphene layers.

We stress the fact that the splitting of the G-band shown in Fig. 23 was not reported in the two other studies of gated bilayer graphene devices [101,103], despite the fact that the G-band observed in reference [101] is clearly asymmetric. Possibly, the splitting shown in Fig. 23 is due to the characteristics of the device which leads to inversion symmetry breaking and allows the observation of the inactive Raman antisymmetric vibration.

5. Raman studies of epitaxial graphene

Raman spectroscopy provides a quick and facile structural and quality characterization of the graphene material that is produced by the epitaxial growth process. This section considers Raman studies on two types of epitaxial graphene. The first type of epitaxial graphene, derived from SiC is discussed in Section 5.1, where it is shown how Raman spectroscopy can be used to characterize few layer graphene grown on Si terminated and on C terminated SiC and separated from the SiC by a carbon buffer layer. In Section 5.2 we consider how Raman spectroscopy can be used to characterize graphene grown by a CVD method based on various transition metal catalysts, most notably Ni. These methods allow for the growth of larger area graphene samples with potential chemical control of many aspects of the growth process. These approaches to the growth of graphene are both at an early stage of development, and detailed Raman characterization could well contribute to a more rapid development of these growth techniques.

5.1. Raman characterization of SiC-derived graphene

Monolayer or few layer graphene, denoted by 1-LG and F-LG, respectively, can be obtained by the annealing of SiC surfaces at high temperatures. Such graphene samples are produced by a graphitization process based on 4H–SiC or 6H–SiC precursors in an ultra-high vacuum process. These two polytype forms of SiC are both hexagonal with a space group C_{6v}^4 or $P6_3mc$ (group #186), while AB Bernal stacked F-LG is described by space group D_{6h}^4 or $P6_3mmc$ (group #194). The layer stacking in 4H–SiC is ABAC while in 6H–SiC it is ABCACB.

Between the SiC structure and the graphene layers, is a monolayer of carbon atoms, called the buffer layer, in which the carbon atoms are in the sp^3 configuration, and these carbon atoms are bonded to the Si atoms. Both carbon-terminated and silicon-terminated surfaces of SiC are used to produce graphene samples. The number of graphene layers in the sample is determined by the temperature (between 1200 and 1600°C, depending on the desired degree of graphitization) and time of the heat treatment process.

Normally, the number of layers N in N -LG is obtained by *in-situ* X-ray photoelectron spectroscopy (XPS), angle-resolved ultra-violet photoemission spectroscopy (ARUPS) or low-energy electron diffraction (LEED), as well as Raman scattering, as discussed in this article (see Section 2). Because of the different symmetry of this buffer layer, it is desirable to transfer

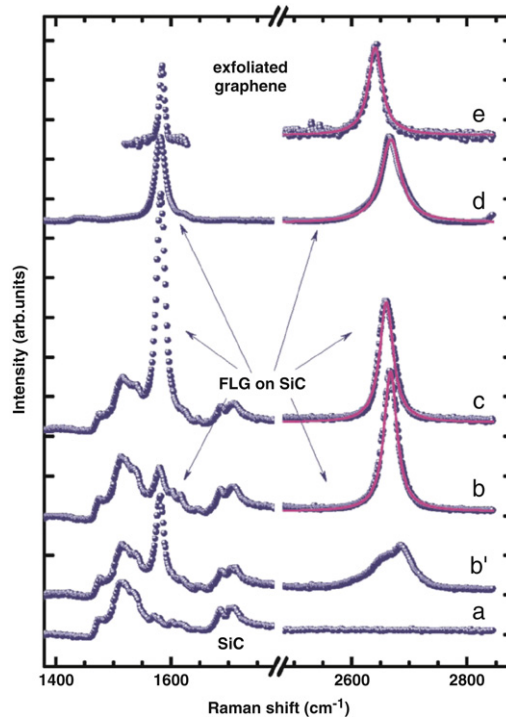


Fig. 24. (a) Raman spectra of a 4H-SiC substrate, (b') of a graphitic residue on the 4H-SiC substrate, (b) of five to ten layers (F-LG) on a 4H-SiC substrate, (c) of another location on the same sample as (b'), (d) for another sample with 70–90 layers of epitaxial graphene, and (e) of mechanically exfoliated graphene. Adapted from Ref. [106].

the graphene sample prepared by this technique to another substrate with spectral features (if any) that are not close in frequency to the graphene G or G' bands.

If the graphene sample remains on the SiC substrate for the Raman characterization procedure, the graphene spectrum must be separated from that for SiC (see Fig. 24). The SiC substrate exhibits a number of second-order Raman features between 1450 and 1750 cm^{-1} , which are superimposed upon the G-band of the graphene sample [106], preventing an accurate analysis of the G-band feature in the graphene spectrum (see Fig. 24). Normally the spectrum of the graphene G-band is obtained by subtracting the spectrum of the SiC substrate from the measured spectrum [107]. Ferralis et al. [108] showed that the intensity of the G-band of graphene can be enhanced with respect to the SiC features by performing a depolarized Raman spectrum, in which the polarization of the scattered light is perpendicular to that of the incident laser beam. This Raman polarization geometry is also appropriate for exciting the E_{2g} symmetry in-plane optical mode in graphite [109].

Faugeras et al. [106] reported a Raman study of the few-layer graphene (F-LG) Raman spectra produced by a C-terminated 4H-SiC surface and showed that, in contrast to the case of few-layer mechanically exfoliated graphenes, the G' band for this C-terminated 4H-SiC derived graphene is composed of a single Lorentzian component centered in the $\omega_{G'}$ range 2655–2665 cm^{-1} (using a 632.8 nm or 1.96 eV laser line) and with a FWHM linewidth of $\sim 60 \text{ cm}^{-1}$. Fig. 24 shows that the shape and FWHM of the G' band is similar to that of turbostratic graphite, (see Section 1.1 and Section 2.5) showing that the few-layer epitaxial graphene sample in Fig. 24 does not exhibit AB Bernal stacking of graphene layers, which is typical of HOPG and of mechanically exfoliated few-layer graphene samples (see Section 2). However, it is claimed [106] in this work that, in contrast to turbostratic graphite where the layers are randomly oriented, the layers in the epitaxial graphene sample produced from a SiC precursor are rotated at specific angles [110–112].

Rohrl et al. [107] observed that the G-band in epitaxial monolayer graphene is significantly blue-shifted, as compared to that from mechanically exfoliated monolayer graphene. These results have been attributed to both the presence of charges and a compressive strain in the sample. From the estimation of the dependence of the G-band peak frequency on the charge transfer, Rohrl et al. [107] concluded that the effect of charging makes a minor contribution to the blue-shift of the G-band, with the main contribution coming from the compressive strain of the sample. According to this work, ω_G decreases with increasing number of graphene layers, tending to the value of ω_G in HOPG (1582 cm^{-1}).

Concerning the G' band, Rohrl et al. [107] observed that the graphene G' band in their samples is composed of a single Lorentzian peak in the case of monolayer graphene, with a FWHM of $\sim 60 \text{ cm}^{-1}$. It was also observed in this work that the position of the peak of the G' band ($\omega_{G'}$) changes from spot to spot on the sample, with spot to spot variations in $\omega_{G'}$ of more than 30 cm^{-1} . By increasing the number of graphene layers, $\omega_{G'}$ decreases and the G' band becomes broader and more asymmetric as the G' band lineshape for graphite (e.g., HOPG) is reached (see Section 2.4). Despite the fact that the

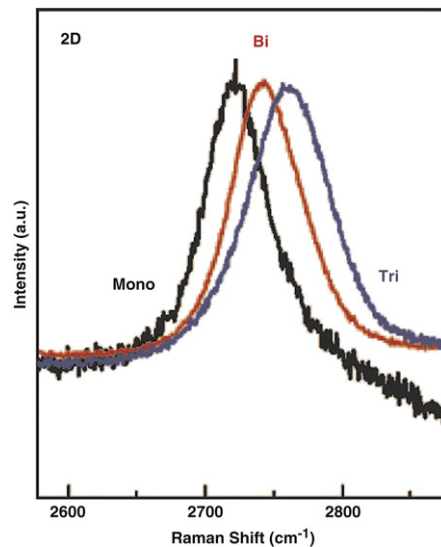


Fig. 25. Raman spectra of monolayer, bilayer and trilayer graphene grown epitaxially on SiC (monolayer, bilayer on 6H-SiC(0001), trilayer on 4H-SiC(0001)). The G' frequency increases with the number of graphene layers. Adapted from Ref. [113].

G' -band for F-LG in this work does not exhibit a clear multi-peak structure, as is observed in mechanically exfoliated graphene, the G' -band for their SiC-based graphene is asymmetric. Rohrl et al. [107] in fact used up to four Lorentzian peaks to fit the G' -band of their normal bilayer graphene sample, as was also used by Ferrari in his lineshape analysis of mechanically exfoliated 2-LG [20].

Lee et al. [113] measured the Raman spectra of monolayer, bilayer and trilayer graphene obtained from the graphitization of Si-terminated SiC. It was observed in this work that the G -band of their epitaxially grown graphene is blue-shifted with respect to that from mechanically exfoliated graphene samples. This result has been attributed to the compressive strain induced by the substrate, which builds up during the cool-down process in the sample preparation.

Fig. 25 shows their G' -band Raman spectra recorded with the 488 nm (or 2.54 eV) laser line for 1-LG, 2-LG, 3-LG samples of graphene thus prepared. The G' -band in this work [113] is always observed at around 2700–2770 cm^{-1} (using the 488 nm laser line), but it is much broader compared to that for mechanically exfoliated graphene samples. In the case of monolayer graphene, the G' -band is fitted by a single Lorentzian with FWHM of $\sim 45 \text{ cm}^{-1}$ and for bilayer and trilayer samples the G' feature becomes still broader ($\sim 65 \text{ cm}^{-1}$ for bilayer graphene prepared from Si-terminated SiC) and the lineshape is asymmetric. However, the multi-peak structure observed for the G' -band in few-layer mechanically exfoliated graphene was not observed in the case of their epitaxial SiC-based few-layer graphene samples. Interestingly, the multi-peak structure of bilayer graphene was somewhat recovered when the epitaxial bilayer sample was transferred to a SiO_2 substrate, showing that the shape of the G' -band in few-layer Si-terminated SiC-based epitaxial F-LG samples is strongly influenced by the SiC substrate and the buffer layer between the graphene and SiC. According to the work reported by Lee et al. [113], the position of the G' -band increases with increasing number of layers (see Fig. 25). Notice that these results are opposite to those reported by Rohrl et al. [107], in which the $\omega_{G'}$ decreases with increasing number of layers.

The main conclusion reported by Lee et al. [113] is the fact that the G' -band FWHM linewidth values exhibit a clear relationship with the inverse of the number of layers. The fact that the FWHM linewidth of epitaxial monolayer graphene (45 cm^{-1}) is significantly larger than that for mechanically exfoliated monolayer graphene (25 cm^{-1}) is attributed in this work to the intrinsic disorder of their epitaxial graphene samples.

A combined Raman and AFM study of epitaxial monolayer graphene grown from a Si-face of 6H-SiC (0001) was recently reported by Robinson et al. [114]. It was shown in this work that both the peak $\omega_{G'}$ value and the lineshape of the G' -band are strongly dependent on the position of the laser spot on the sample. Using an experimental setup in which the laser spot was reduced to about 300 nm, these authors were able to observe a G' -band with a FWHM $\sim 25 \text{ cm}^{-1}$, which is similar to the value found in mechanically exfoliated monolayer graphene (see Section 2). The different values for $\omega_{G'}$ were correlated with the topography of the substrate, leading the authors to conclude that the variations of the G' -band position ($\omega_{G'}$) are due to strain inhomogeneities of their monolayer graphene samples. This effect is shown in Fig. 26 where three consecutive spectra of the G' -band are collected at different spots on the sample separated by 300 nm. The middle curve is fitted by a sum of the two Lorentzians, that fit the top and bottom spectra, respectively. These results show that the middle Raman spectrum is collected over two areas of monolayer graphene subjected to different amounts and types of strain [114].

It is clear that there are still today many open questions concerning the Raman spectra of epitaxial graphene grown on SiC. Many of the contradictory results found in the literature, concerning the peak frequency, the lineshape of the Raman G and G' bands, and the dependence of these bands on the number of layers are related to the strong influence of the compressive strain induced by the lattice mismatch difference in the thermal expansion coefficients of SiC and graphene. Moreover, it

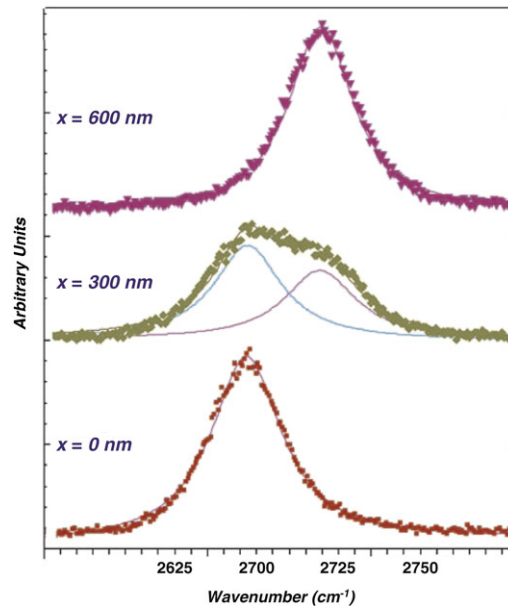


Fig. 26. Three consecutive spectra collected in a line scan of the G' band at 2.33 eV laser excitation for 1-LG obtained from SiC-based epitaxial graphene. The top and bottom spectra are fit by a single Lorentzian and the middle curve is fitted to a sum of the same Lorentzians associated with the two adjacent points on this Raman line scan. Adapted from Ref. [114].

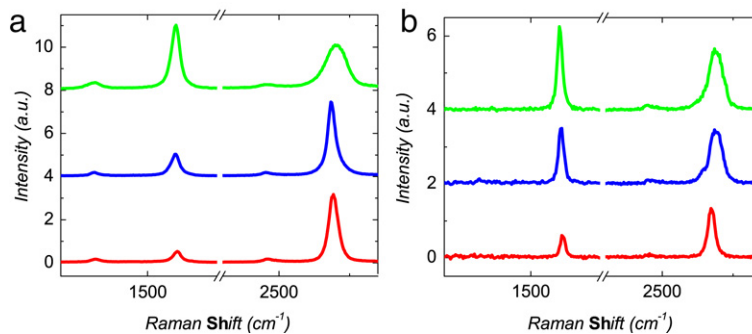


Fig. 27. (a) Raman spectra of 1-LG (red), 2-LG (blue), 3-LG (green) prepared by a CVD process based on a Ni(111) precursor and then transferred to a SiO_2/Si substrate. (b) Raman spectra of 1-LG (red), 2-LG (blue), 3-LG (green) prepared by the mechanical exfoliation of HOPG, shown for comparison. All spectra were taken with $E_{\text{laser}} = 2.33$ eV. Adapted from Ref. [31].

has been demonstrated that the detailed Raman lineshape depends on the fact that the precursor materials can be 4H-SiC or 6H-SiC, or can be a SiC surface that is either carbon or silicon terminated. Furthermore, since in many samples the lateral sizes are smaller than $1 \mu\text{m}$, normal micro-Raman experiments, in which the size of the laser spot is about $1 \mu\text{m}$, probe inhomogeneous parts of the sample, thereby broadening the Raman bands compared to those from mechanically exfoliated graphene. It is, however, clear that the G' -band of epitaxial few-layer graphene derived from SiC is more similar to that of turbostratic graphite than to HOPG, showing that the graphene layers in epitaxial graphene are not stacked in the AB (or Bernal) configuration. As the synthesis of SiC-based epitaxial graphene improves, it may be possible to obtain further information about the more detailed non-Bernal stacking order that has been discussed for Si-terminated and C-terminated SiC-based epitaxial F-LG samples, and the differences between their structures from one another.

5.2. Raman characterization of CVD grown graphene

Another method under development for the preparation of few-layer epitaxial graphene is by the chemical vapor deposition (CVD) growth from thin films of transition metals which serve as catalysts for the growth of few layer graphene (F-LG). Examples of transition metals that have been used successfully for the growth of F-LG are Co [115], Pt [116,117], Ir [118, 119], Ru [120,121] and Ni [31,122–126]. In the case of Ni, the in-plane lattice constant in the 111 plane is $a = 0.232$ nm, as compared to graphite (for which $a = 0.246$ nm) at room temperature, representing a lattice mismatch of 5.6% for this CVD growth. This lattice match is sufficient to allow continuous growth of graphene films on the surface of the Ni and these films

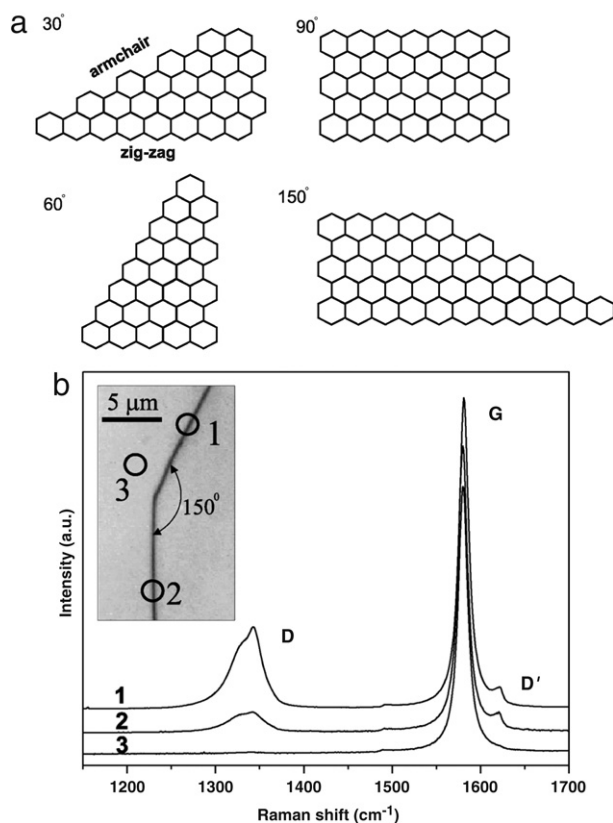


Fig. 28. (a) Different types of edges that can be formed by cutting the graphene plane at different angles. (b) Raman spectra obtained in three different regions of the HOPG sample from Ref. [131]. The laser energy was 1.96 eV. The inset shows a schematic diagram of the edge step and the regions where spectra 1, 2, and 3 were taken (open circles). Adapted from Ref. [131].

exhibit a large fraction of 1-LG and 2-LG domains, with regions up to 20 μm in size, large enough for Raman characterization of each of these graphene regions individually.

The Raman spectra of 1-LG, 2-LG and 3-LG derived from CVD growth using the Ni precursor and from mechanically exfoliated HOPG are shown in Fig. 27 for spectra excited at $E_{\text{laser}} = 2.33$ eV. A low intensity of the disorder-induced *D* band (1350 cm^{-1}) is observed relative to that of the *G*-band (1585 cm^{-1}) for the monolayer sample with peak intensity ratios (I_D/I_G) in the range $0.05 < I_D/I_G < 0.3$ for the CVD-derived sample. The *D*-band intensity largely comes from graphene edges and sub-domain boundaries in areas with a constant number of graphene layers. Spectra from the thinnest sections of the CVD graphene film show a sharp linewidth (38 cm^{-1}) and a single Lorentzian profile of the *G'* band ($\sim 2693\text{ cm}^{-1}$), which are hallmarks of monolayer graphene (see Section 2.1). Although the *G'* lineshape provides a good measure of the number of layers in the case of HOPG-mechanically exfoliated graphene, the *G'* lineshape for multilayer CVD grown graphene shows some variation between regions of identical numbers of layers. Moreover, regions of 2-LG and 3-LG, as identified by AFM measurements, show *G'*-band features described by a single Lorentzian and with linewidths of ($\sim 30\text{--}83\text{ cm}^{-1}$). This indicates a departure from the ordered AB stacking and therefore the corresponding electronic coupling between graphene layers does not occur in all regions of the film. Transmission electron microscope (TEM) diffraction measurement of the interlayer spacing yields a value of $0.350 \pm 0.014\text{ nm}$ for folded-over regions of these F-LG samples, consistent with interlayer spacings in the turbostratic regime (see Section 1.1), though the sharp spot diffraction patterns (rather than rings) indicate local interlayer stacking order. From the Raman and TEM observations, we conclude that there is local stacking order but the stacking is neither AB Bernal stacking nor turbostratic random stacking. The decreased interlayer coupling may have advantages for some practical applications since incommensurate multilayer graphene with weak interlayer coupling can have electronic properties more similar to those of a single sheet of graphene. Furthermore, instead of the *G'* lineshape, it was found that the *G* to *G'* peak intensity ratios ($I_G/I_{G'}$) provide a good correlation with the number of graphene layers in the CVD-derived graphene samples [31]. Correlation between the grains in the Ni polycrystalline precursor and the grains in the resulting graphene films suggest that some annealing of the initial Ni films might produce larger single domain graphene regions in CVD grown graphene.

Raman characterization of CVD grown 2-LG [127] based on a Ru(0001) catalytic precursor was also carried out. Though no Raman spectra were obtained from 1-LG similarly prepared, the 2-LG sample showed a single *G'*-band Lorentzian peak with a linewidth of 42 cm^{-1} and both the *G*-band and *G'*-band spectral features were homogeneous throughout a spatial

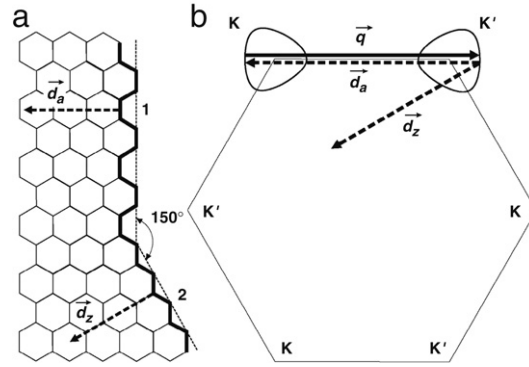


Fig. 29. (a) Schematic illustration of the atomic structure of the graphene edges shown in Fig. 28 emphasizing the different structures along the armchair and zigzag edges. (b) First Brillouin zone of 2D graphene, showing that the intervalley double resonance mechanism satisfies conservation of momentum for an armchair graphite edge but not for a zigzag edge. Adapted from Ref. [19].

scan of the 2-LG sample. The authors noted a surprising similarity between the Raman spectrum for this 2-LG sample (as determined by scanning probe measurements) with a comparison spectrum for a monolayer reference graphene sample prepared by the mechanical exfoliation process taken with the same experimental set-up. In this comparison, their 2-LG sample showed frequency upshifts of 13 cm^{-1} and 4 cm^{-1} , respectively, for the G and G' band peak frequencies, and an increase of 4 cm^{-1} in the FWHM linewidth of the G' band, though the $(I_{G'}/I_G)$ intensity ratio for the CVD derived 2-LG film appeared to be notably smaller than that for their monolayer comparison spectrum. Similarities can also be seen between the $(I_{G'}/I_G)$ intensity ratio for the CVD derived 2-LG samples from the Ru (0001) precursor [120,121], on one hand, and the CVD-derived 2-LG derived from the Ni (111) precursor [31]. Another similarity found for these two types of 2-LG CVD grown graphene samples was that both types of samples showed spot diffraction patterns, indicative of interlayer ordering, but with departures from the Bernal AB interlayer stacking order.

6. Raman studies of graphene and graphite edges

In this section we consider the use of Raman spectroscopy to distinguish between armchair and zigzag edges because an edge breaks the symmetry of the graphene structure and gives rise to D -band intensity (see Section 1.3). Different wave vectors are involved for the armchair and zigzag edges, and this allows Raman spectroscopy to distinguish between these edges.

Knowledge about graphene edges is of great importance, since the electronic properties of nanometer scale graphene materials are sensitive to the specific types of edges [128–130]. Furthermore, Raman spectroscopy can be used to measure the quality of the edges in graphene, namely, the armchair and zigzag edges. Fig. 28 shows armchair and zigzag edges and the possible combination of angles between either of them, which are multiples of 30° . The first study of graphene edges by Raman spectroscopy was done on step-like edges in graphite [131]. Fig. 28(b) shows the Raman spectra from three different locations on such a sample, where it is possible to clearly identify those edges that have a 150° angle between them. For the laser spot positions number 1 and 2, it is possible to observe two disorder-induced Raman bands, the D -band (1340 cm^{-1}) and the D' -band (1620 cm^{-1}). For position 3, where the Raman spectra were taken from a flat interior region of the HOPG sample, no disorder-induced bands were found, indicating the absence of imperfect crystalline order [131]. Whereas the D' intensities are the same for positions 1 and 2, the D band intensity is different for these two locations.

Cançado et al. [131] showed, using scanning tunneling microscopy (STM) characterization, that position 2 is indeed a zigzag edge and that the weaker D band intensity with respect to that for the armchair edge is due to the one-dimensional character of a defect along the edges. From the intervalley double resonance mechanism which gives rise to the D band (see Section 1.3), we see in Fig. 29(b) that the phonon wavevector is \mathbf{q} . Thus, in order to conserve momentum, when the electron is scattered back elastically from K' to K in the Brillouin zone by a phonon with wavevector $\mathbf{d} = -\mathbf{q}$. Fig. 29(a) shows the armchair and zigzag edges with their respective defect wavevectors \mathbf{d}_a and \mathbf{d}_z , which are perpendicular to the armchair and zigzag edges. Fig. 29(b) shows the first Brillouin zone of graphene, oriented in accordance with the real space lattice [Fig. 29(a)]. Here we see that the armchair wavevector (\mathbf{d}_a) is able to participate in the intervalley double resonance process between the K and K' points. On the other hand, the zigzag defect wavevector (\mathbf{d}_z) cannot connect the K and K' points, and thus the elastic electron scattering by the defect does not have enough momentum for spanning points K and K' and for conserving momentum as shown in the figure for the DR Raman process (Fig. 29(b)). This result shows that only armchair edges and not zigzag edges are expected to exhibit a D band in the Raman spectra of a perfect graphene edge [131].

The D' band, which originates from an intravalley process connecting k points around the same K (or K') point, can satisfy momentum conservation for either armchair or zigzag edges. Thus, the D' band is independent of the edge structure, as is observed experimentally in Fig. 28(b).

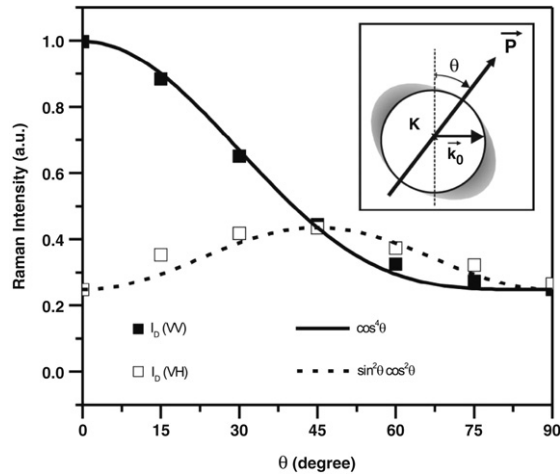


Fig. 30. Dependence of the D band intensity on the polarization direction of the incident and scattered light. The spectra were taken in region 1 in Fig. 28 (armchair edge) at room temperature. The laser power density on the sample was 3×10^5 W/cm² and the laser energy was 2.41 eV. The inset shows a schematic illustration of the optical anisotropy around the K point of 2D graphite [69], where θ is the angle between the light polarization \mathbf{P} and the armchair edge direction. Figure from Ref. [131].

Moreover the Raman scattering from these edges exhibit a polarization dependence for both the incident and scattered light polarizations. Because of optical anisotropy in graphene [69], the optical absorption (emission) is proportional to $|\mathbf{P} \times \mathbf{k}|$, where \mathbf{P} is the polarization of the incident (scattered) light and \mathbf{k} is the wavevector of the electron measured from the K point. Thus in the case of the VV and VH polarization configurations (where V and H , respectively, denote the vertical and horizontal polarization directions for the light), the intensity of the D band is given by $I_D(VV) \propto \cos^4(\theta)$ and $I_D(VH) \propto \cos^2(\theta) \sin^2(\theta)$, where θ is the angle of the incident light with respect to \mathbf{k} [131]. The experimental points in Fig. 30 show the measured polarization dependence for the armchair edge D band intensity (square points) which is compared with the theoretical curves (lines) for both the VV (closed squares and solid lines) and VH (open squares and dashed lines) configurations. The corresponding result was also verified for the G' band for graphene, where the one-dimensional nature of the double resonance mechanism along the high symmetry lines $\Gamma-K-M-K'-\Gamma$ also gives rise to a polarization dependence [132].

The same results found by Cançado et al. [131] at step edge defects in graphite are also expected to be seen in graphene. Although *mechanically exfoliated graphene* of top of silicon oxide appears to have sharp edges macroscopically, these edges are found to be imperfect at the atomic level, as seen by high resolution electron microscopy. You et al. [133] performed a series of Raman imaging experiments of the D band in different graphene samples and showed that, indeed, when the edges have an angle of $n \times 30^\circ$ (for $n = 1$ and 3) between them, the D band intensity is more pronounced for one of the edges. Fig. 31 shows two different graphene edges where the intensity difference of the D band is sufficient to distinguish between the armchair and zigzag edges. In fact, this result depends sensitively on the quality of the edges that can be made by the mechanical exfoliation of graphite [133]. Casiraghi et al. [134] showed that the difference between the D band intensity for different edges is not always large enough to be correlated reliably with the edge orientation. Although Raman spectroscopy can potentially provide a useful tool to probe the edge chirality of graphene, imperfect graphene edges produced by the mechanical cleavage of graphite can produce ambiguous results that do not clearly discriminate the armchair and zigzag edges from one another [134].

7. Raman studies of graphene nanoribbons

Graphene is a two dimensional, zero gap semiconductor. For electronics applications it is desirable to have a semiconductor with an energy gap to realize high ON/OFF ratios in transistor devices [27], and this is where nanoribbons may play an important role. By cutting a graphene sheet into ribbons a few nanometers wide, it is possible to form a gap in the electronic dispersion relations due to the confinement of the electron wavefunction [128,129,135]. Moreover, the width and chirality of the edges of the nanoribbons define the size of the bandgap [129,135]. Fig. 32(a) and (b) illustrate the structures of zigzag and armchair nanoribbons, respectively, while Fig. 32(c) shows a tight binding calculation of the electronic density of states for a narrow zigzag nanoribbon with $N = 6$ [see Fig. 32(a)] [129]. Tight binding calculations [129] suggest that all zigzag ribbons are metallic while armchair ribbons can be either semiconducting or metallic, depending on the number of columns of carbon atoms N along the width w_a [see Fig. 32(d)] [129], and some STM measurements show experimental evidence in support of these phenomena [136]. A more complete calculation including many-body effects by Son et al. [135] found that armchair and zigzag nanoribbons are all semiconducting [see Fig. 32(e)] [135].

Raman spectroscopy can be used as a fast and non-destructive method to localize and probe nanoribbon properties. Cançado et al. [7] performed Raman spectroscopy measurements on nanographite ribbons sitting on top of an HOPG

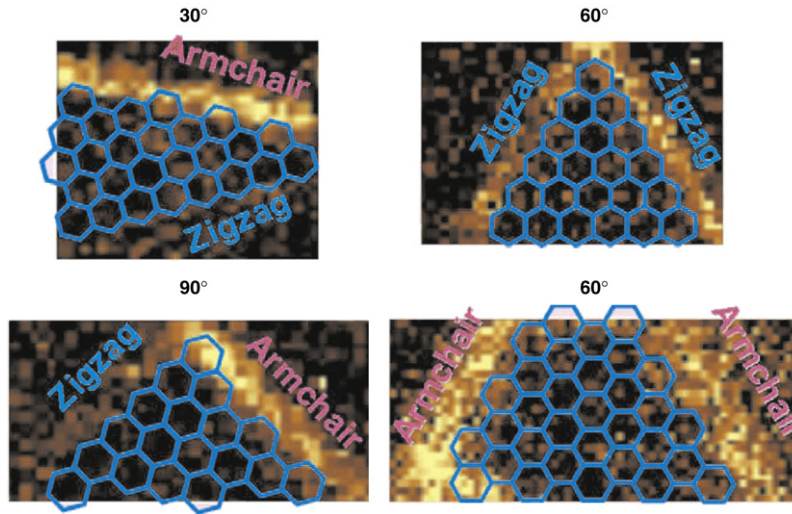


Fig. 31. Raman mapping of the D band intensity for four different types of angles between the graphene edges. It is possible to observe that the D band intensity is enhanced at the armchair edges, and zigzag edges are found to have a smaller intensity when compared to the armchair edges. Figure adapted from Ref. [133].

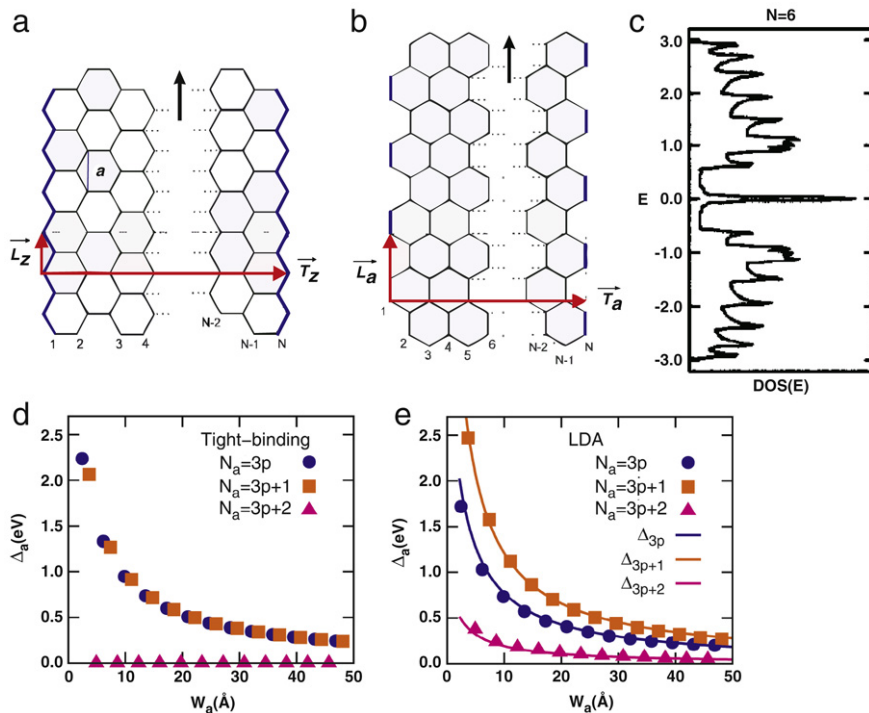


Fig. 32. (a) and (b) Geometrical structure of a zigzag and an armchair graphene ribbon, respectively. (c) Tight binding calculation of the density of states for a zigzag ribbon with $N = 6$ (see (a)), (d) and (e) Calculated dependence of the energy gap on the width of armchair nanoribbons using a tight binding calculation (d) and a first principles (LDA) calculation (e), respectively. The figure is adapted from Ref. [135].

(highly oriented pyrolytic graphite) substrate. Fig. 33(a) shows an atomic force microscopy (AFM) image of several parallel nanoribbons with an average width of 8 nm, with lengths that can be as large as 1 μm . Fig. 33(b) shows an AFM height profile on one of these nanoribbons, confirming that the nanoribbon is one graphene layer thick and has a width of 8 nm. Fig. 33(c) shows Raman spectra taken on this nanoribbon with 2.41 eV laser energy in the region of the G band. Here it is possible to observe two G peaks in the spectra, the G_1 feature (with a dotted curve) centered at 1568 cm^{-1} and the G_2 peak (with a solid curve) at 1579 cm^{-1} . As discussed in Ref. [7] the frequency of the G_1 peak is strongly dependent on the laser power density used in the experiment.

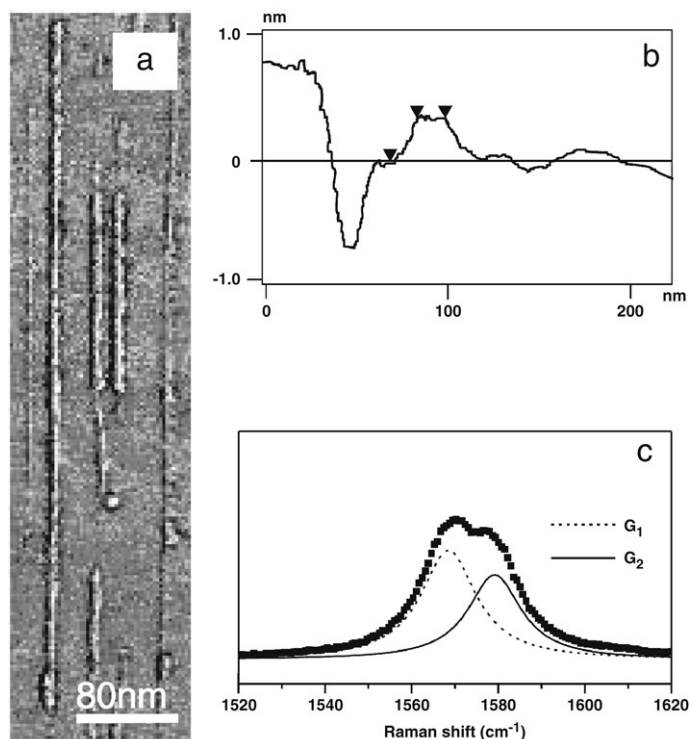


Fig. 33. (a) AFM image of different ribbons parallel with each other. (b) An AFM height profile for one of the nanoribbons, showing a step high of 0.35 nm. (c) Raman spectra in the G band region showing a two peak feature consisting of the G₁ (dotted lines) and G₂ (full lines) Raman bands. This figure was adapted from Ref. [7].

To clearly establish the physical origin of these two G band features, polarized Raman spectra were taken [7]. Fig. 34(a) shows the Raman spectra for different polarization angles with respect to the nanoribbon, where $\theta = 0^\circ$ denotes the light polarization vector \mathbf{P} parallel with the ribbon. The G₁ peak intensity decreases gradually from parallel ($\theta = 0^\circ$) to perpendicular ($\theta = 90^\circ$) polarization with respect to the nanoribbon length axis [Fig. 34(b)]. On the other hand, the G₂ peak intensity is not affected by the polarization angle [see Fig. 34(a)]. It can therefore be concluded from Fig. 34(b) that the G₁ Raman peak is associated with the G band of the nanoribbon [7]. The separation in frequency between the G₁ and G₂ peaks arises from the laser heating of the nanoribbon due to the lower thermal conductivity from the graphene ribbon to the HOPG substrate on which the nanoribbon sits. This angular dependence in Fig. 34(b) is explained by considering the optical anisotropy of graphene [69] and the quantum confinement in a 1D graphene ribbon, which has been discussed by Ref. [7]. It is interesting to note, that the G₁ peak intensity for the nanoribbon can be even larger than that for the G₂ feature which originates from the HOPG substrate. Although the number of carbon atoms within the laser spot size of the HOPG sample is at least 100 times larger than the number of C atoms in the ribbon, the signal from the graphene ribbon is, nevertheless, clearly observed. The observation of such a strong signal means that the laser energy should be close to an optical transition associated with the van Hove singularities in the valence and conduction bands of the nanoribbons [7].

Subsequent to the above studies carried out in 2004, isolated graphene nanoribbons have been fabricated on a silicon oxide substrate. Two types of fabrication techniques have been applied: structural etching [137] of mechanically exfoliated graphene or chemical routes to exfoliate graphite [138]. The chemically exfoliated graphite is obtained by intercalating graphite flakes with sulfuric acid and nitric acid and then heating at $\sim 1000^\circ\text{C}$ in forming gas (Ar + 10% H₂) for 1 min, resulting in an exfoliated graphite [5, 138]. The latter method produces ribbons with small widths (< 10 nm) with an average length of $1\ \mu\text{m}$ [138]. Fig. 35(a)–(c) shows different ribbons imaged by AFM with different widths on top of a silicon oxide substrate. This Raman measurement in Fig. 35(d) for the G band is one of the few reported in the literature thus far for isolated carbon nanoribbons. One of the major difficulties impeding progress in this area is sample preparation to yield isolated nanoribbons with well-defined edges and chiralities.

The paucity of experimental Raman studies in the literature is partly compensated for by recent theoretical investigations of the Raman modes of nanoribbons [136, 139–143]. Fig. 36 shows a calculation of the nanoribbon first-order Raman spectra for different ribbon widths [141]. The armchair nanoribbon Raman spectra with 7 and 8 carbon dimer widths is given in Fig. 36(a) and (b), respectively, while Fig. 36(c) and (d) show the corresponding Raman spectra for a zigzag nanoribbon. It is interesting to compare these spectra with the Raman spectra of a single wall carbon nanotube (SWNT), where the most prominent features are the low frequency radial breathing mode (RBM) and the G band in the $1580\text{--}1590\ \text{cm}^{-1}$ range. In Fig. 36 it is possible to distinguish three intense modes for carbon nanoribbons, the R, E and L modes using the notation of Ref.

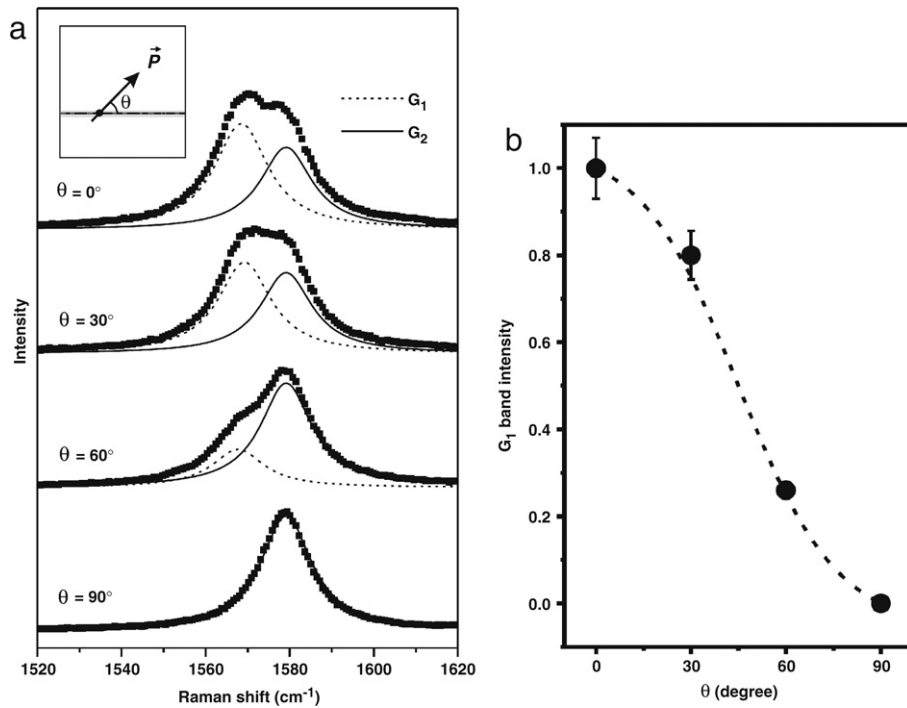


Fig. 34. (a) Raman spectra obtained for different values of the light polarization angles (θ) with respect to the nanoribbon direction or its length. (b) Intensity of the G_1 peak associated with the nanoribbon as a function of the angle θ (see insert to (a) which defines θ as the angle between the ribbon axis and the polarization vector). This figure was adapted from Ref. [7].

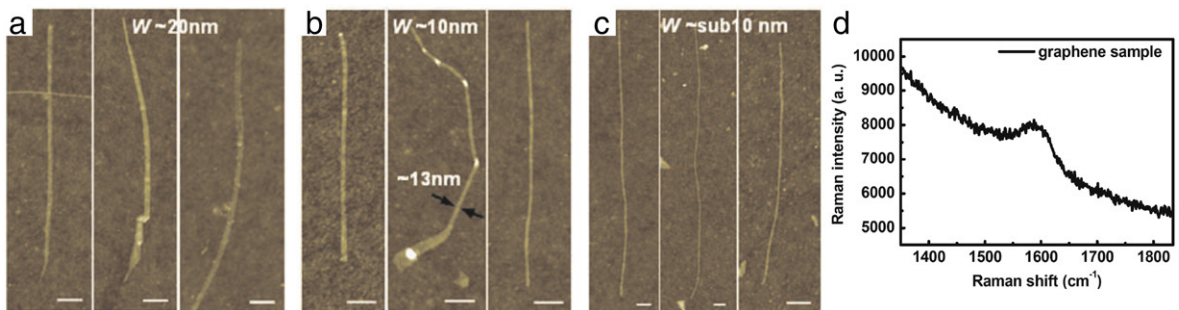


Fig. 35. (a)–(c) AFM images of graphene ribbons for different widths on top of a silicon oxide substrate. The scale bar is 100 nm. (d) Raman spectrum for the G-band in a graphene nanoribbon < 10 nm in width. This figure was adapted from Ref. [138].

[141]. The E mode is an E_{2g} -like vibration in the nanoribbon network which gives rise to the G band in the Raman spectra for graphene. The R mode for the nanoribbon is a radial breathing-like mode (RBLM) resembling the radial breathing mode of carbon nanotubes. This mode is created by the vibration of the outer atoms, while the center atoms are almost static [141]. The localized L mode in Fig. 36 is a mode generated by the vibration of the atoms at the edge of the ribbons [141]. Both the RBLM and the localized modes are very useful for characterizing the nanoribbon properties by Raman spectroscopy as is usually done in single wall carbon nanotubes (SWNTs). First, the RBLM mode frequency depends on the width of the nanoribbon [141,143], the larger the width, the lower the RBLM frequency. The localized mode can be different for different types of edges, thus making a distinction between armchair and zigzag edges, as is seen in Fig. 36.

Although experimental Raman studies on carbon nanoribbons are still lacking in the literature, we highlighted here the importance of resonance phenomena and polarized Raman spectroscopy to clearly distinguish nanoribbons relative to graphite or graphene [7]. On the other hand, a significant amount of theoretical effort has already been made to provide a framework that can be used to probe nanoribbon properties by Raman spectroscopy [139–143]. One can then envision the development of a Kataura-like plot for nanoribbons, which would provide a powerful tool to identify the chirality and width of individual nanoribbons by Raman spectroscopy, as has been done for single wall carbon nanotubes [6,77,144].

Recent advances [145–147] in the synthesis of large scale quantities (grams per day) of crystalline graphene nanoribbon material (Fig. 37(a) and (b)) by a CVD process, with nanoribbon widths of 20–300 nm, and thicknesses of 2–40 graphene

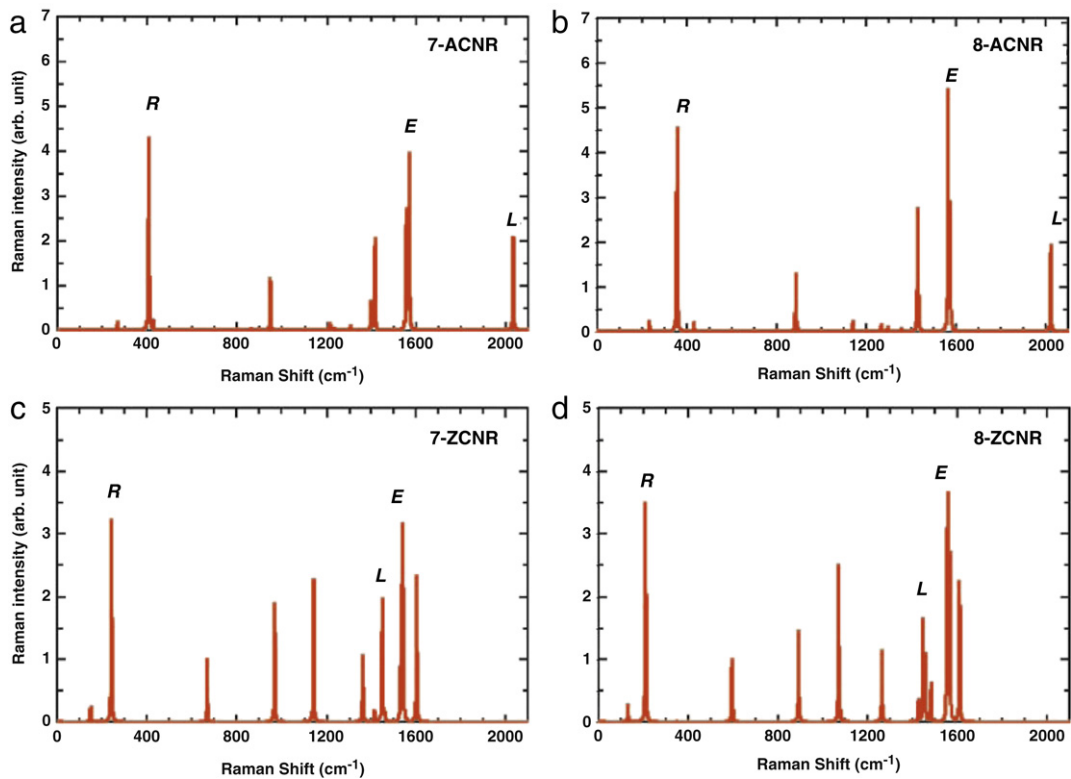


Fig. 36. (a), (b) Calculated Raman spectra of armchair nanoribbons (ACNR) for 7 and 8 carbon dimers, respectively. (c)–(d) The same corresponding spectra as in (a), (b) but now for zigzag nanoribbons (ZCNR). The most prominent modes in the spectra are marked as *R* for the radial breathing-like mode (RBLM) mode, *E* for the G band, and *L* for the localized mode. Figure adapted from Ref. [141].

layers [145], have shown how to produce atomically sharp zigzag and armchair edges (Fig. 37(c)) by the joule heating of these as-grown nanoribbons (see Fig. 37(a)) within an integrated TEM-STM instrument [145–147]. The transmission electron microscope (TEM) allows imaging of the graphene ribbon while manipulating the ribbon and using the scanning tunneling microscope (STM) to make current–voltage measurements. Parallel TEM and Raman studies of this material under static heat treatment at constant temperature also results in the annealing of defects within the interior of the ribbons (Fig. 37(d) and (e)) but for heat treatment temperatures of 1500 °C and above, adjacent edges tend to form loops (Fig. 37(e)) to passivate their reactive dangling bonds [147]. Raman spectra for the as-prepared material and for the material heat treated at various heat treatment temperatures are shown in Fig. 37(f), where a decrease in *D*-band intensity can be identified by the decrease in the in-plane disorder, but a residual *D*-band intensity remains at high heat treatment temperature (2800 °C) and is attributed to the presence of edge loops [147]. This approach to the preparation of graphene nanoribbons is at an early stage of development and offers promise as a method to study the development and motion of edges and their electronic and transport properties. Raman spectroscopy is expected to play a major role in guiding the future development of this graphene nanoribbon material.

8. Summary and conclusions

In summary, we have presented an overview of the Raman spectroscopy in graphene, discussing the theoretical background associated with the first-order and the double resonance Raman scattering mechanisms that gives rise to the main features in the Raman spectra of graphene, and presenting some recent Raman studies in different types of graphene, including both exfoliated and epitaxial graphene samples. Symmetry considerations based on a Group Theory analysis were presented and the selection rules associated with the different Raman features were discussed. We showed that Raman spectroscopy is a very useful tool to determine the number of layers in few-layer graphene, and in particular to distinguish monolayer from few-layer graphene stacked in the Bernal (AB) configuration.

The Raman features of different types of graphene samples were compared with those of two extreme cases—the ordered 3D crystalline graphite where all layers are stacked in the Bernal (AB) configuration and turbostratic graphite, in which the layers are stacked with rotational disorder. We showed that, in contrast to the case of mechanically exfoliated graphene where the Raman spectra are well understood, the Raman studies of epitaxial graphene are still at an early stage. It is clear that in SiC-based epitaxial graphene, the Raman features are strongly dependent on the precursor material and on the strain

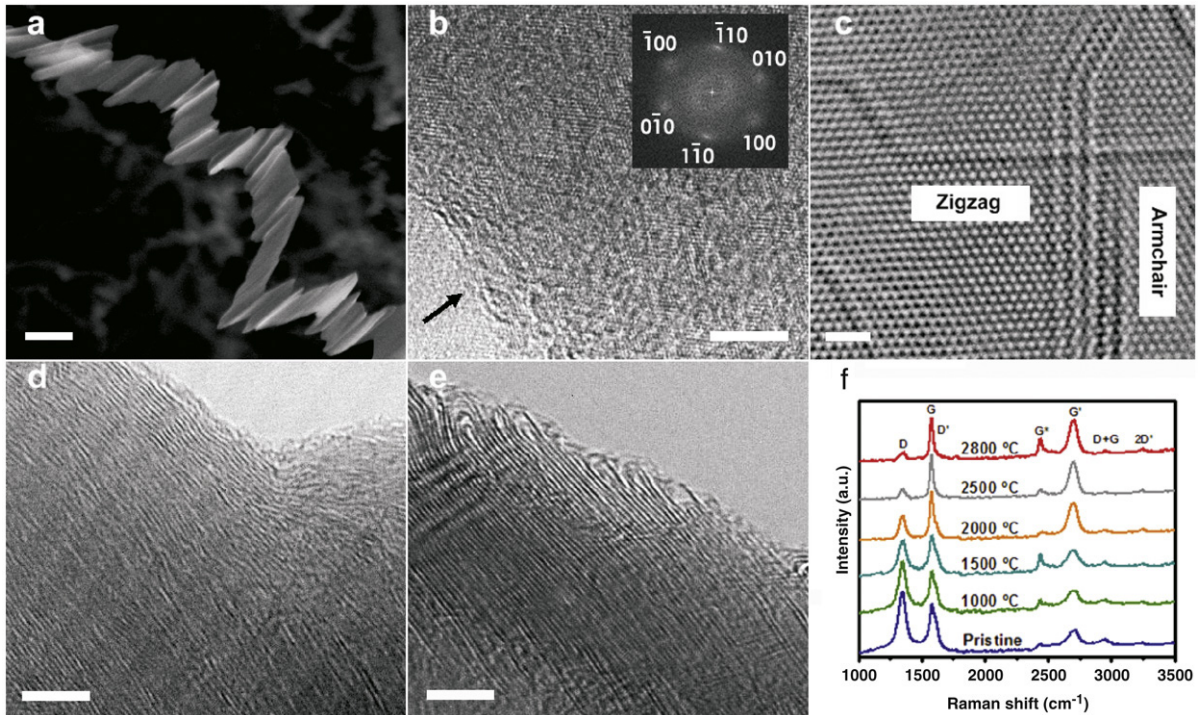


Fig. 37. (a) SEM image of an as-produced graphene ribbon (scale bar = 500 nm) (b) HRTEM image of the surface and edge of an as-produced ribbon, where the arrow indicates the edge (scale bar = 4 nm). The inset shows the FFT of this region where the hexagonal pattern of a honeycomb structure is evident. (c) HRTEM image of the same sample after the Joule heating experiment (scale bar = 1 nm), (d) and (e) HRTEM images of the edges of a pristine sample and a sample heat treated at 2000 °C, respectively (scale bar = 5 nm), (f) micro Raman spectra on bulk nanoribbons heat treated at various temperatures taken with $E_{\text{laser}} = 2.33$ eV [145,147].

of the graphene due to interaction with the substrate. As the quality of graphene samples improves, Raman spectroscopy will likely play a role in illuminating the properties of graphene close to the Dirac point, using freely suspended samples.

We have also presented Resonance Raman studies of graphene, where the energy of the excitation laser line can be tuned continuously. Due to the double-resonance Raman mechanism, photons with different energies interact with electrons and phonons with different wavevectors. Therefore, by changing the energy of the excitation laser, it is possible to probe the dispersion of electrons and phonons near the Dirac point of graphene. In particular, a resonant Raman investigation of the G' band allows the determination of the tight-binding parameters in bilayer graphene. These Raman results agrees well with infrared absorption and transmission spectroscopy of bilayer graphene which also reveals electron-hole asymmetry [148].

The electron–phonon interaction is very strong in graphene, and the adiabatic (Born–Oppenheimer) approximation fails for this system. Some special phonons, specially those responsible for the main Raman features, can create an electron–hole pair, and this process renormalizes the phonon energy giving rise to the so-called Kohn anomaly. This process is suppressed when the Fermi level position is changed by an amount greater than half of the phonon energy. Experimental results in monolayer and bilayer graphene, where the position of the Fermi level is tuned by applying a gate voltage or using electrochemical methods, were discussed and compared with theoretical predictions.

The possibility of distinguishing between armchair and zig-zag graphene edges was discussed in terms of the double-resonance Raman process, showing that the scattering at an armchair edge gives a strong D -band intensity while a weak D -band feature is observed at a zigzag edge. This result can be used to test the atomic quality of a graphene edge. Finally, we discussed polarized Raman studies in graphene nanoribbons in which the signal is enhanced due to resonance with singularities in the density of electronic states. In the future, Raman spectroscopy is likely to play a significant role in illuminating the special one-dimensional properties of narrow graphene nanoribbons.

Acknowledgments

LMM and MAP acknowledge the support from the Brazilian Network on Carbon Nanotube Research and the Brazilian Agencies CNPq and FAPEMIG. The MIT authors acknowledge support under NSF Grants No. DMR 07-04197 and CTS-05-06830. The authors are grateful to Professor Riichiro Saito and Dr. Jie Jiang of Tohoku University and to Alfonso Reina of MIT and Professor A. Jorio of UFMG for useful suggestions regarding the contents of this review. The authors wish to acknowledge the hospitality of the International Center for Theoretical Physics in Trieste, Italy which hosted the Graphene Week 2008 and provided the inspiration that led to the writing of this review article.

References

- [1] K.S. Novoselov, A.K. Geim, S.V. Morozov, D. Jiang, M.I. Katsnelson, I.V. Grigorieva, S.V. Dubonos, A.A. Firsov, *Science* 306 (2004) 666–669.
- [2] K.S. Novoselov, D. Jiang, F. Schedin, T.J. Booth, V.V. Khotkevich, A.K. Morozov, S.V. Geim, *Proc. Natl. Acad. Sci.* 102 (2005) 10451–10453.
- [3] K.S. Novoselov, A.K. Geim, S.V. Morozov, D. Jiang, M.I. Katsnelson, I.V. Grigorieva, S.V. Dubonos, A.A. Firsov, *Nature* 438 (2005) 197–200.
- [4] Y. Zhang, Y.W. Tan, H.L. Stormer, P. Kim, *Nature* 438 (2005) 197.
- [5] M.S. Dresselhaus, G. Dresselhaus, K. Sugihara, I.L. Spain, H.A. Goldberg, *Graphite Fibers and Filaments*, in: Springer Series in Materials Science, vol. 5, Springer-Verlag, Berlin, 1988.
- [6] M.S. Dresselhaus, G. Dresselhaus, R. Saito, A. Jorio, *Phys. Rep.* 409 (2005) 47–99.
- [7] L.G. Cançado, M.A. Pimenta, R.A. Neves, G. Medeiros-Ribeiro, T. Enoki, Y. Kobayashi, K. Takai, K. Fukui, M.S. Dresselhaus, R. Saito, A. Jorio, *Phys. Rev. Lett.* 93 (2004) 047403.
- [8] R. Saito, G. Dresselhaus, M.S. Dresselhaus, *Physical Properties of Carbon Nanotubes*, Imperial College Press, London, 1998.
- [9] F. Tuinstra, J.L. Koenig, *J. Phys. Chem.* 53 (1970) 1126.
- [10] F. Tuinstra, J.L. Koenig, *J. Compos. Mater.* 4 (1970) 492.
- [11] R.J. Nemanich, S.A. Solin, *Solid State Commun.* 23 (1977) 417.
- [12] R.J. Nemanich, S.A. Solin, *Phys. Rev. B* 20 (1979) 392–401.
- [13] R.P. Vidano, D.B. Fishbach, L.J. Willis, T.M. Loehr, *Solid State Commun.* 39 (1981) 341.
- [14] P. Lespade, A. Marchand, M. Couzi, F. Cruege, *Carbon* 22 (1984) 375.
- [15] P. Lespade, R. Al-Jishi, M.S. Dresselhaus, *Carbon* 20 (1982) 427–431.
- [16] D.S. Knight, W.B. White, *J. Mater. Res.* 4 (1989) 385.
- [17] H. Wilhelm, M. Lelausian, E. McRae, B. Humbert, *J. Appl. Phys.* 84 (1998) 6552–6558.
- [18] A.C. Ferrari, J. Robertson, *Phys. Rev. B* 61 (2000) 14095.
- [19] M.A. Pimenta, G. Dresselhaus, M.S. Dresselhaus, L.G. Cançado, A. Jorio, R. Saito, *Phys. Chem. Chem. Phys.* 9 (2007) 1276–1291.
- [20] A.C. Ferrari, J.C. Meyer, V. Scardaci, C. Casiraghi, M. Lazzeri, M. Mauri, S. Piscanec, Da Jiang, K.S. Novoselov, S. Roth, A.K. Geim, *Phys. Rev. Lett.* 97 (2006) 187401; A.C. Ferrari, *Solid State Commun.* 143 (2007) 47.
- [21] J.-C. Charlier, P.C. Eklund, J. Zhu, A.C. Ferrari, in: Ado Jorio, M.S. Dresselhaus, G. Dresselhaus (Eds.), *Electron and Phonon Properties of Graphene: Their Relationship with Carbon Nanotubes, Topics in the Synthesis, Structure, Properties and Applications*, in: Springer Series on Topics in Applied Physics, vol. 111, Springer-Verlag, Berlin, 2007, pp. 673–709 (Chapter 21).
- [22] A.H. Castro Neto, F. Guinea, N.M.R. Peres, K.S. Novoselov, A.K. Geim, *Rev. Modern Phys.* 81 (2009) 109–161.
- [23] Ni Zhenhua, Y. Wang, T. Yu, Z. Shen, *Nano Res.* 1 (4) (2008) 273–291.
- [24] A. Gupta, G. Chen, P. Joshi, S. Tadigadapa, P.C. Eklund, *Nano Lett.* 6 (2006) 2667.
- [25] D. Graf, F. Molitor, K. Ensslin, C. Stampfer, A. Jungen, C. Hierold, L. Wirtz, *Nano Lett.* 7 (2007) 238.
- [26] A.W. Moore, in: P.L. Walker, P.A. Throver (Eds.), *Chemistry and Physics of Carbon*, Marcel Dekker Inc., New York, 1981, p. 233. vol. 17.
- [27] A.K. Geim, K.S. Novoselov, *Nature Mater.* 6 (2007) 183.
- [28] A.M. Affoune, B.L.V. Prasad, H. Sato, T. Enoki, Y. Hishiyama, Y. Kaburagi, *Chem. Phys. Lett.* 348 (2001) 17.
- [29] C. Berger, Z.M. Song, X. Lee, Xiaosong Wu, Nate Brown, Cile Naud, Didier Mayou, Tianbo Li, Joanna Hass, Alexei N. Marchenkov, Edward H. Conrad, Phillip N. First, Walt A. de Heer, *Science* 312 (2006) 1191–1196.
- [30] Claire Berger, Zhimin Song, Tianbo Li, Xuebin Li, Asmerom Y. Ogbazghi, Rui Feng, Zhenting Dai, Alexei N. Marchenkov, Edward H. Conrad, Phillip N. First, Walt A. de Heer, *J. Phys. Chem. B* 108 (2004) 19912.
- [31] A. Reina, X. Jia, J. Ho, D. Nezich, H. Son, V. Bulovich, M.S. Dresselhaus, J. Kong, *Nano Lett.* 9 (2009) 30–35.
- [32] X. Du, I. Skachko, A. Barker, E.Y. Andrei, *Nature Nanotechnol.* 3 (2008) 491.
- [33] M. Lazzeri, C. Attacalite, L. Wirtz, Francesco Mauri *Phys. Rev. B* 78 (2008) 081406.
- [34] K.A. Wang, A.M. Rao, P.C. Eklund, M.S. Dresselhaus, G. Dresselhaus, *Phys. Rev. B* 48 (1993) 11375–11380.
- [35] M.S. Dresselhaus, R.A. Jishi, G. Dresselhaus, D. Inomata, K. Nakao, Riichiro Saito, *Mol. Mater.* 4 (1994) 27–40.
- [36] Mildred S. Dresselhaus, Gene Dresselhaus, Ado Jorio, *Group Theory: Application to the Physics of Condensed Matter*, Springer, Berlin, 2008.
- [37] J. Jiang, R. Saito, Ge.G. Samsonidze, S.G. Chou, A. Jorio, G. Dresselhaus, M.S. Dresselhaus, *Phys. Rev. B* 72 (2005) 235408–1–11.
- [38] J. Maultzsch, S. Reich, C. Thomsen, H. Requardt, P. Ordejón, *Phys. Rev. Lett.* 92 (2004) 075501.
- [39] Ge.G. Samsonidze, E.B. Barros, R. Saito, J. Jiang, G. Dresselhaus, M.S. Dresselhaus, *Phys. Rev. B* 75 (2007) 155420.
- [40] W. Kohn, *Phys. Rev. Lett.* 2 (1959) 393.
- [41] S. Piscanec, M. Lazzeri, M. Mauri, A.C. Ferrari, J. Robertson, *Phys. Rev. Lett.* 93 (2004) 185503.
- [42] M. Ramsteiner, J. Wagner, *Appl. Phys. Lett.* 51 (1987) 1355.
- [43] I. Pócsik, M. Hundhausen, M. Koós, L. Ley, *J. Non-Cryst. Solids* 227–230 (1998) 1083–1086.
- [44] M.J. Matthews, M.A. Pimenta, G. Dresselhaus, M.S. Dresselhaus, M. Endo, *Phys. Rev. B* 59 (1999) R6585.
- [45] A.V. Baranov, A.N. Bekhterev, Y.S. Bobovich, V.I. Petrov, *Opt. Spectrosk.* 62 (1987) 1036.
- [46] C. Thomsen, S. Reich, *Phys. Rev. Lett.* 85 (2000) 5214.
- [47] R. Saito, A. Jorio, A.G. Souza Filho, G. Dresselhaus, M.S. Dresselhaus, M.A. Pimenta, *Phys. Rev. Lett.* 88 (2002) 027401.
- [48] R. Saito, A. Grüneis, Ge.G. Samsonidze, V.W. Brar, G. Dresselhaus, M.S. Dresselhaus, A. Jorio, L.G. Cançado, C. Fantini, M.A. Pimenta, A.G. Souza Filho, *New J. Phys.* 5 (2003) 157.1–157.15.
- [49] J. Maultzsch, S. Reich, C. Thomsen, *Phys. Rev. B* 70 (2004) 155403.
- [50] J. Jiang, R. Saito, K. Sato, J.S. Park, Ge.G. Samsonidze, A. Jorio, G. Dresselhaus, M.S. Dresselhaus, *Phys. Rev. B* 75 (2007) 035405.
- [51] G. Ge, Samsonidze, *Photophysics of carbon nanotubes*, Ph.D. Thesis, Department of Electrical Engineering and Computer Science, Massachusetts Institute of Technology, February 2007.
- [52] D.L. Mafra, G. Samsonidze, L.M. Malard, D.C. Elias, J.C. Brant, F. Plentz, E.S. Alves, M.A. Pimenta, *Phys. Rev. B* 76 (2007) 233407.
- [53] S. Reich, C. Thomsen, *Philos. Trans. R. Soc.* 362 (2004) 2271–2288.
- [54] J. Kürti, V. Zólyomi, A. Grüneis, H. Kuzmany, *Phys. Rev. B* 65 (2002) 165433(1–9).
- [55] J.S. Park, Alfonso Reina Cecco, R. Saito, J. Jiang, G. Dresselhaus, M.S. Dresselhaus, *Carbon* 47 (2009) 1303–1310.
- [56] L.M. Malard, M.H.D. Guimarães, D.L. Mafra, M.S.C. Mazzoni, A. Jorio, *Phys. Rev. B* 79 (2009) 125426.
- [57] S.K. Saha, U.V. Waghmare, H.R. Krishnamurthy, A.K. Sood, *Phys. Rev. B* 78 (2008) 165421.
- [58] J. Jiang, H. Tang, B. Wang, Z. Su, *Phys. Rev. B* 77 (2008) 235421.
- [59] J. Jiang, R. Saito, A. Grüneis, S.G. Chou, Ge.G. Samsonidze, A. Jorio, G. Dresselhaus, M.S. Dresselhaus, *Phys. Rev. B* 71 (2005) 205420.
- [60] A.H. Castro Neto, F. Guinea, *Phys. Rev. B* 75 (2007) 045404.
- [61] R. Narula, S. Reich, *Phys. Rev. B* 78 (2008) 165422.
- [62] R. Saito, A. Jorio, A.G. Souza Filho, G. Dresselhaus, M.S. Dresselhaus, M.A. Pimenta, *Phys. Rev. Lett.* 88 (2002) 027401.
- [63] L.M. Malard, J. Nilsson, D.C. Elias, J.C. Brant, F. Plentz, E.S. Alves, A.H. Castro Neto, M.A. Pimenta, *Phys. Rev. B* 76 (2007) 201401.
- [64] C. Thomsen, S. Reich, J. Maultzsch, *Philos. Trans. R. Soc. Lond. A* 362 (2004) 2337.
- [65] J.W. McClure, *Phys. Rev.* 108 (1957) 612.
- [66] J.C. Slonczewski, P.R. Weiss, *Phys. Rev.* 109 (1958) 272.
- [67] B. Partoens, F.M. Peeters, *Phys. Rev. B* 74 (2006) 075404.
- [68] L.G. Cançado, A. Reina, J. Kong, M.S. Dresselhaus, *Phys. Rev. B* 77 (2008) 245408.

- [69] A. Grüneis, R. Saito, Ge.G. Samsonidze, T. Kimura, M.A. Pimenta, A. Jorio, A.G. Souza Filho, G. Dresselhaus, M.S. Dresselhaus, *Phys. Rev. B* 67 (2003) 165402–1–1–65402–7.
- [70] L.G. Cançado, M.A. Pimenta, R. Saito, A. Jorio, L.O. Ladeira, A. Grüneis, A.G. Souza-Filho, G. Dresselhaus, M.S. Dresselhaus, *Phys. Rev. B* 66 (2002) 035415.
- [71] L.G. Cançado, K. Takai, T. Enoki, M. Endo, Y.A. Kim, H. Mizusaki, N.L. Speziali, A. Jorio, M.A. Pimenta, *Carbon* 46 (2008) 272.
- [72] L.G. Cançado, K. Takai, T. Enoki, M. Endo, Y.A. Kim, H. Mizusaki, A. Jorio, L.N. Coelho, R. Magalhães-Paniago, M.A. Pimenta, *Appl. Phys. Lett.* 88 (2006) 163106.
- [73] Z. Ni, Y. Wang, T. Yu, Y. You, Zexiang Shen *Phys. Rev. B* 77 (2008) 235403.
- [74] P. Poncharal, A. Ayari, T. Michel, J.-L. Sauvajol, *Phys. Rev. B* 77 (2008) 235403.
- [75] J.M.B. Lopes dos Santos, N.M.R. Peres, A.H. Castro Neto, *Phys. Rev. Lett.* 99 (2007) 256802.
- [76] S. Latil, V. Meunier, L. Henrard, *Phys. Rev. B* 76 (2007) 201402(R).
- [77] C. Fantini, A. Jorio, M. Souza, M.S. Strano, M.S. Dresselhaus, M.A. Pimenta, *Phys. Rev. Lett.* 93 (2004) 147406.
- [78] A.C. Ferrari, J. Robertson, *Phys. Rev. B* 64 (2001) 075414.
- [79] L.M. Malard, D. Nishide, L.G. Dias, Rodrigo B. Capaz, A.P. Gomes, A. Jorio, C.A. Achete, R. Saito, Y. Achiba, H. Shinohara, M.A. Pimenta, *Phys. Rev. B* 76 (2007) 233412.
- [80] R.A. Jishi, M.S. Dresselhaus, G. Dresselhaus, K. Wang, P. Zhou, A.M. Rao, P.C. Eklund, *Chem. Phys. Lett.* 206 (1993) 187.
- [81] G. Benedek, G. Onida, *Phys. Rev. B* 47 (1993) 16471.
- [82] A. Grüneis, R. Saito, T. Kimura, L.G. Cançado, M.A. Pimenta, A. Jorio, A.G. Souza Filho, G. Dresselhaus, M.S. Dresselhaus, *Phys. Rev. B* 65 (2002) 155405.
- [83] O. Dubay, G. Kresse, *Phys. Rev. B* 67 (2003) 035401.
- [84] G.G. Samsonidze, R. Saito, A. Jorio, A.G. Souza Filho, A. Grüneis, M.A. Pimenta, G. Dresselhaus, M.S. Dresselhaus, *Phys. Rev. Lett.* 90 (2003) 027403.
- [85] V.N. Popov, P. Lambin, *Phys. Rev. B* 73 (2006) 085407.
- [86] R. Nicklow, N. Wakabayashi, H.G. Smith, *Phys. Rev. B* 5 (1972) 4951.
- [87] J.L. Wilkes, R.E. Palmer, R.F. Willis, *J. Electron Spectrosc. Relat. Phenom.* 44 (1987) 355.
- [88] C. Oshima, T. Aizawa, R. Souda, Y. Ishizawa, Y. Sumiyoshi, *Solid State Commun.* 65 (1988) 1601.
- [89] S. Siebentritt, R. Pues, K.-H. Rieder, A.M. Shikin, *Phys. Rev. B* 55 (1997) 7927–7934.
- [90] M. Mohr, J. Maultzsch, E. Dobardžić, S. Reich, I. Milošević, M. Damnjanović, A. Bosak, M. Krisch, C. Thomsen, *Phys. Rev. B* 76 (2007) 035439.
- [91] L.M. Malard, J. Nilsson, D.L. Maffra, D.C. Elias, J.C. Brant, F. Plentz, E.S. Alves, A.H. Castro Neto, M.A. Pimenta, *Phys. Status Solidi b* 245 (2008) 2060–2063.
- [92] N.B. Brandt, S.M. Chudinov, Ya.G. Ponomarev, *Semimetals 1: Graphite and its Compounds, North-Holland, Amsterdam, 1988.*
- [93] M. Lazzeri, S. Piscanec, Francesco Mauri, A.C. Ferrari, J. Robertson *Phys. Rev. B* 73 (2006) 155426.
- [94] T. Ando, *J. Phys. Soc. Jpn.* 75 (2006) 024707.
- [95] Eduardo V. Castro, K.S. Novoselov, S.V. Morozov, N.M.R. Peres, J.M.B. Lopes dos Santos, Johan Nilsson, F. Guinea, A.K. Geim, A.H. Castro, *Neto Phys. Rev. Lett.* 99 (2007) 216802.
- [96] M. Lazzeri, F. Mauri, *Phys. Rev. Lett.* 97 (2006) 266407.
- [97] T. Ando, in: Ado Jorio, M.S. Dresselhaus, G. Dresselhaus (Eds.), *Role of the Aharonov-Bohm Phase in the Optical Properties of Carbon Nanotubes, Topics in the Synthesis, Structure, Properties and Applications*, in: Springer Series on Topics in Applied Physics, vol.111, Springer-Verlag, Berlin, 2007, pp. 213–232 (Chapter 4).
- [98] A. Das, S. Pisana, B. Chakraborty, S. Piscanec, S.K. Saha, U.V. Waghmare, K.S. Novoselov, H.R. Krishnamurthy, A.K. Geim, A.C. Ferrari, A.K. Sood, *Nature Nanotechnol.* 3 (2008) 210.
- [99] S. Pisana, M. Lazzeri, C. Casiraghi, K.S. Novoselov, A.K. Geim, A.C. Ferrari, F. Mauri, *Nature Mater.* 6 (2007) 198.
- [100] J. Yan, Y. Zhang, P. Kim, A. Pinczuk, *Phys. Rev. Lett.* 98 (2007) 166802.
- [101] Jun Yan, Erik A. Henriksen, Philip Kim, Aron Pinczuk, *Phys. Rev. Lett.* 101 (2008) 136804.
- [102] L.M. Malard, D.C. Elias, E.S. Alves, M.A. Pimenta, *Phys. Rev. Lett.* 101 (2008) 257401.
- [103] A. Das, B. Chakraborty, S. Piscanec, A.K. Sood, A.C. Ferrari, 2008, *cond-mat arXiv: 0807.1631*.
- [104] T. Ando, *J. Phys. Soc. Japan* 75 (2006) 124701.
- [105] G. Dresselhaus, M.S. Dresselhaus, *Phys. Rev.* 140 (1965) A401–A412.
- [106] C. Augeras, A. Nerrire, M. Potemski, A. Mahmood, E. Dujardin, C. Berger, W.A. de Heer, *Appl. Phys. Lett.* 92 (2008) 011914.
- [107] J. Rohrl, M. Hundhausen, K.V. Emtsev, Th. Seyller, R. Graupner, L. Ley, *Appl. Phys. Lett.* 92 (2008) 201918.
- [108] N. Ferralis, R. Maboudian, C. Carraro, *Phys. Rev. Lett.* 101 (2008) 156801.
- [109] M.S. Dresselhaus, G. Dresselhaus, *Light Scattering in Solids III* 51 (1982) 3–57; M. Cardona, G. Güntherodt (Eds.), *Topics in Applied Physics Springer-Verlag, Berlin.*
- [110] J. Hass, R. Feng, T. Li, X. Li, Z. Zong, W.A. de Heer, P.N. First, E.H. Conrad, C.A. Jeffrey, C. Berger, *Appl. Phys. Lett.* 89 (2006) 143106.
- [111] J. Hass, R. Feng, J.E. Millan-Otoya, X. Li, M. Sprinkle, P.N. First, W.A. de Heer, E.H. Conrad, C. Berger, *Phys. Rev. B* 75 (2007) 214109.
- [112] J. Hass, F. Varchon, J.E. Millan-Otoya, M. Sprinkle, N. Sharma, W.A. de Heer, C. Berger, P.N. First, L. Magaud, E.H. Conrad, *Phys. Rev. B* 100 (2008) 125504.
- [113] D.S. Lee, C. Riedl, B. Krauß, K. von Klitzing, U. Starke, J.H. Smet, *Nano Lett.* 8 (2008) 4320–4325.
- [114] J.A. Robinson, C.P. Pulls, N.E. Staley, J. Stitt, M.A. Fanton, K.V. Emtsev, T. Seyller, Y. Liu, *Nano Lett.* 9 (2009) 964–968.
- [115] J. Vaari, J. Lahtinen, P. Hautojrvi, The adsorption and decomposition of acetylene on clean and K-covered Co(0001), *Catal. Lett.* 44 (1) (1997) 43–49.
- [116] H. Ueta, M. Saida, C. Nakai, Y. Yamada, M. Sasaki, S. Yamamoto, Highly oriented monolayer graphite formation on Pt(1 1 1) by a supersonic methane beam, *Surf. Sci.* 560 (1–3) (2004) 183–190.
- [117] D.E. Starr, E.M. Pazhetnov, A.I. Stadrnichenko, A.I. Boronin, S.K. Shaikhutdinov, Carbon films grown on Pt(1 1 1) as supports for model gold catalysts, *Surf. Sci.* 600 (13) (2006) 2688–2695.
- [118] N. Gall, E. Rutkov, A. Tontegode, Interaction of silver atoms with iridium and with a two-dimensional graphite film on iridium: Adsorption desorption and dissolution, *Phys. Solid State* 46 (2) (2004) 371–377.
- [119] J. Coraux, A.T. Ndiaye, C. Busse, T. Michely, Structural Coherency of Graphene on Ir(111), *Nano Lett.* 8 (2) (2008) 565–570.
- [120] A.L.V. de Parga, F. Calleja, B. Borca, J.M.C.G. Passeggi, J.J. Hinarejos, F. Guinea, R. Miranda, Periodically rippled graphene: Growth and spatially resolved electronic structure, *Phys. Rev. Lett.* 100 (5) (2008) 056807–4.
- [121] S. Marchini, S. Gunther, J. Winterlin, Scanning tunneling microscopy of graphene on Ru(0001), *Phys. Rev. B* 76 (7) (2007) 075429–9.
- [122] D.W. Goodman, J.T. Yates, CO isotopic mixing measurements on nickel: Evidence for irreversibility of CO dissociation, *J. Catalysis* 82 (2) (1983) 255–260.
- [123] H.H. Madden, J. Koppers, G. Ertl, Interaction of carbon monoxide with (110) nickel surfaces, *J. Chem. Phys.* 58 (8) (1973) 3401–3410.
- [124] Y. Gamo, A. Nagashima, M. Wakabayashi, M. Terai, C. Oshima, Atomic structure of monolayer graphite formed on Ni(111), *Surf. Sci.* 374 (1–3) (1997) 61–64.
- [125] T. Kawano, M. Kawaguchi, Y. Okamoto, H. Enomoto, H. Bando, Preparation of layered B/C/N thin films on nickel single crystal by LPCVD, *Solid State Sci.* 4 (11–12) (2002) 1521–1527.
- [126] A.G. Starodubov, M.A. Medvetskii, A.M. Shikin, V.K. Adamchuk, Intercalation of silver atoms under a graphite monolayer on Ni(111), *Phys. Solid State* 46 (7) (2004) 1340–1348.
- [127] P.W. Sutter, J.-I. Flege, E.A. Sutter, Epitaxial graphene on ruthenium, *Nat. Mater.* 7 (5) (2008) 406–411.
- [128] M. Fujita, K. Wakabayashi, K. Nakada, K. Kusakabe, *J. Phys. Soc. Japan* 65 (1996) 1920.
- [129] K. Nakada, M. Fujita, G. Dresselhaus, M.S. Dresselhaus, *Phys. Rev. B* 54 (1996) 17954.
- [130] Y. Miyamoto, K. Nakada, M. Fujita, *Phys. Rev. B* 59 (1999) 9858.

- [131] L.G. Cançado, M.A. Pimenta, B.R. Neves, M.S. Dantas, A. Jorio, Influence of the atomic structure on the Raman spectra of graphite edges, *Phys. Rev. Lett.* 93 (2004) 247401.
- [132] D. Yoon, H. Moon, Y.-W. Son, G. Samsonidze, B.H. Park, J.B. Kim, Y.P. Lee, H. Cheong, *Nano Lett.* 8 (2008) 4270–4274.
- [133] Y. You, Z. Ni, T. Yu, Z. Shen, *Appl. Phys. Lett.* 93 (2008) 163112.
- [134] C. Casiraghi, A. Hartschuh, H. Qian, S. Piscanec, C. Georgi, A. Fasoli, K.S. Novoselov, D.M. Basko, A.C. Ferrari, *Nano Lett.* 9 (2009) (in press).
- [135] Y.-W. Son, M.L. Cohen, S.G. Louie, *Phys. Rev. Lett.* 97 (2006) 216803.
- [136] T. Enoki, Y. Kobayashi, K.-I. Fukui, *Internat. Rev. Phys. Chem.* 26 (2007) 609–645.
- [137] M.Y. Han, B. Ozyilmaz, Y.B. Zhang, P. Kim, *Phys. Rev. Lett.* 98 (2007) 206805.
- [138] X. Li, X. Wang, L. Zhang, S. Lee, H. Dai, *Science* 319 (2008) 1229.
- [139] T. Kawai, Y. Miyamoto, O. Sugino, Y. Koga, *Phys. Rev. B* 62 (2000) R16349.
- [140] T. Tanaka, A. Tajima, R. Mariuzumi, M. Hosoda, R. Ohno, E. Rokuta, C. Oshima, S. Otani, *Solid State Commun.* 123 (2002) 33.
- [141] J. Zhou, J. Dong, *Appl. Phys. Lett.* 191 (2007) 173108.
- [142] M. Yamada, Y. Yamakita, K. Ohno, *Phys. Rev. B* 77 (2008) 054302.
- [143] M. Vandescuren, P. Hermet, V. Meunier, L. Henrard, Ph. Lambin, *Phys. Rev. B* 78 (2008) 195401.
- [144] M.S. Dresselhaus, G. Dresselhaus, R. Saito, A. Jorio, in: S.R. Leone, J.T. Groves, R.F. Ismagilov, G. Richmond (Eds.), *Annual Reviews of Physical Chemistry Chemical Physics*, Annual Reviews, Palo Alto, CA, 2007, pp. 719–747.
- [145] Jessica Campos-Delgado, Jose Manuel Romo-Herrera, Xiaoting Jia, David Cullen, H. Muramatsu, Y.A. Kim, T. Hayashi, Z. Ren, D.J. Smith, O. Okuno, T. Ohba, H. Kanoh, K. Kaneko, M. Endo, H. Terrones, M.S. Dresselhaus, M. Terrones, *Nano Lett.* 8 (2008) 2773–2778.
- [146] Xiaoting Jia, Mario Hofmann, Vincent Meunier, Bobby G. Sumpter, Jessica Campos-Delgado, José Manuel Romo-Herrera, Hyungbin Son, Ya-Ping Hsieh, Alfonso Reina, Jing Kong, Mauricio Terrones, Mildred S. Dresselhaus, *Science* 323 (2009) 1701–1705.
- [147] Jessica Campos-Delgado, Y.A. Kim, T. Hayashi, A. Morelos-Gomez, M. Hofmann, H. Muramatsu, M. Endo, H. Terrones, R.D. Shull, M.S. Dresselhaus, M. Terrones, *Chem. Phys. Lett.* 469 (2009) 177–182.
- [148] Z.Q. Li, E.A. Henriksen, Z. Jiang, Z. Hao, M.C. Martin, P. Kim, H.L. Stormer, D.N. Basov, *Phys. Rev. Lett.* 102 (2009) 037403.